Unprecedented polyvinyl polymer loading on SWCNTs in the liquid phase

Leshan Usgodaarachchi[1,2], Eleftheria Zelou[1,2], Vikraman Haribaskar[2], Yuchen Yang[2], Eftychia Grana[3], Nicolas Battaglini[2], Samia Zrig[2], Eric Cloutet[3], Benoit Piro[2], Bérengère Lebental[1,*]

[1] Université Gustave Eiffel, COSYS/IMSE, 14-20 boulevard Newton, Champs sur Marne, 77447 Marne-la-Vallée Cedex 2, France

[2] Université Paris Cité, ITODYS, CNRS, F-75006 Paris, France

[3] University of Bordeaux, CNRS, Bordeaux INP, LCPO, UMR 5629, 16 Av. Pey Berland, 33600 Pessac, France

Corresponding author: berengere.lebental@univ-eiffel.fr

S1 Polymer synthesis- NMR and SEC data

Figure 1, Figure 2 and Figure 3 provide the NMR data for the polymers PVIm, PVT and PVKdac, respectively. Their synthesis is described in section 2.1.2 of the main paper. Figure 4 provides the SEC data for PVKdac.

^{1}H NMR of PVIm (400 MHz, DMF-d_7) □□ (ppm) 8-7 (m, 3H), 4.6-4.4 and 2.8-2.4 (m, 3H), 1.5-1.0 (m, 3H).

^{1}H NMR of PVT (400 MHz, DMF-d_7) of PVT □ (ppm) 9.4-9.0 (m, 2H), 4.3-4.0 and 3.2-2.5 (m, 3H), 1.5-1.2 (m, 3H).

^{1}H NMR of PVKdac (400 MHz, CH_2Cl_2) d (ppm) 8.5–5.7 (m, 6H), 5.0–4.0 (m, 3H), 3.5–2.9 (m, 1H), 3.0–1.5 (m, 2H)

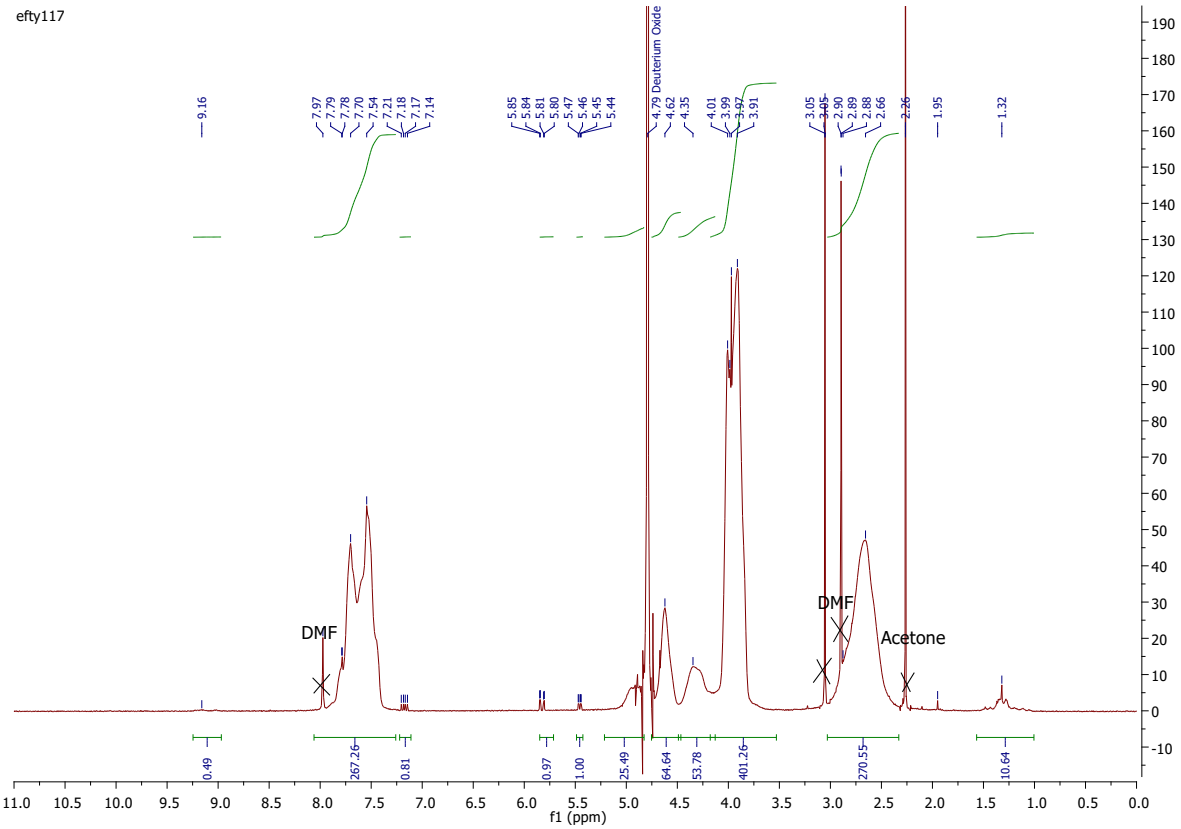

Figure 1: ^{1}H NMR (400 MHz, DMF-d_7) data for Poly (1-methyl-3-vinylimidazolium iodide) (PVIm)

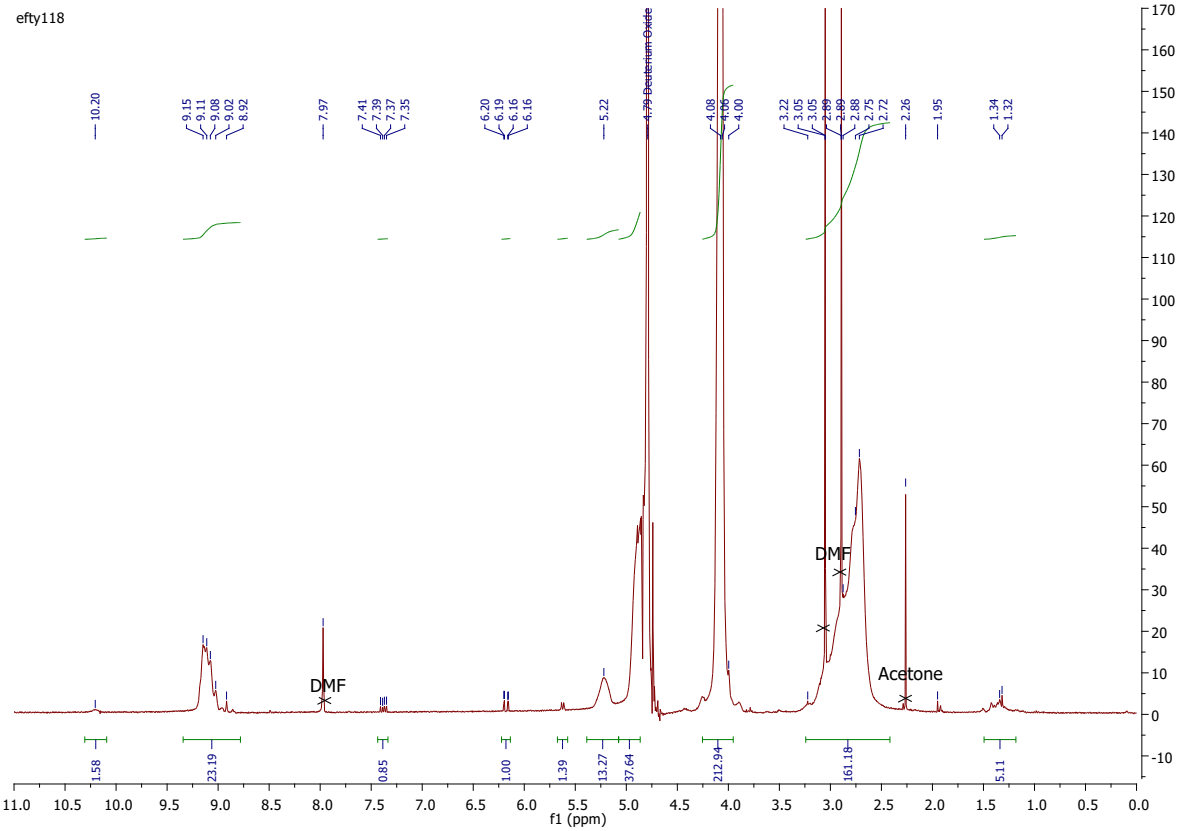

Figure 2: ^{1}H NMR (400 MHz, DMF-d_7) data for Poly (4-methyl-1-vinyl-1,2,4-triazolium iodide) (PVT)

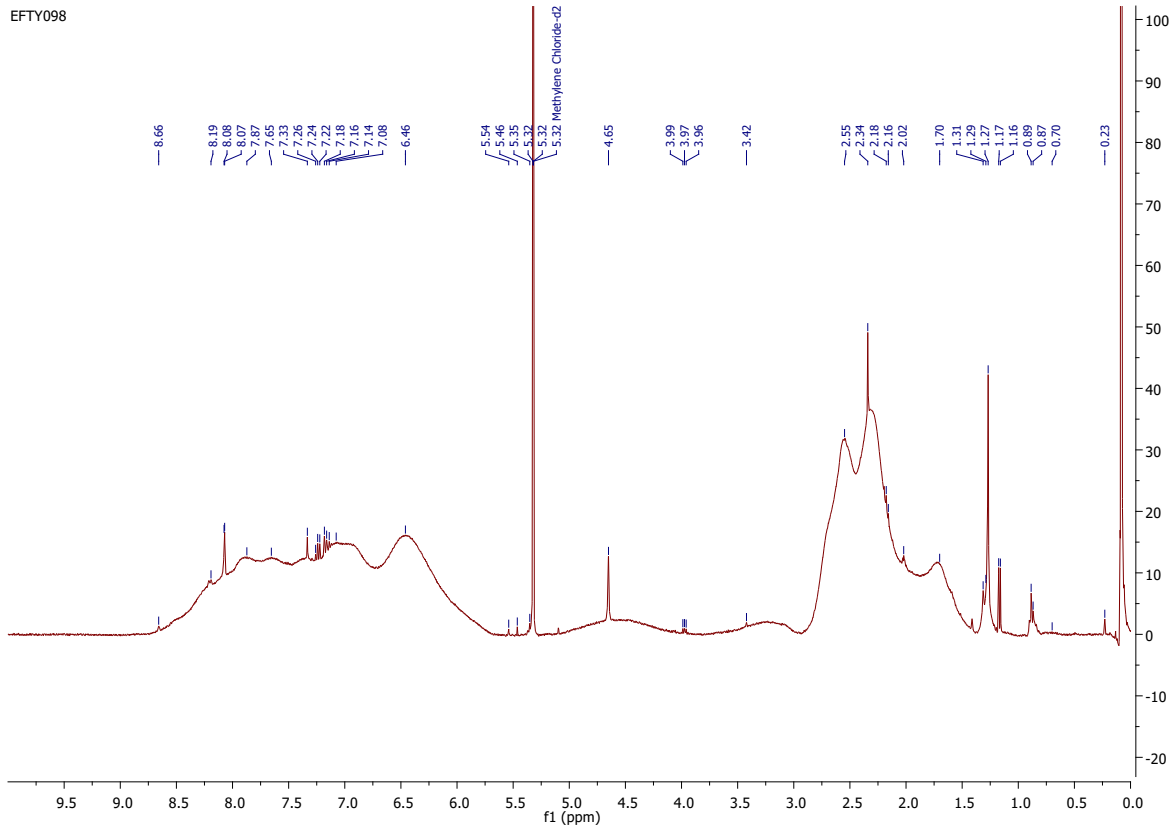

Figure 3: ^{1}H NMR of PVKdac (400 MHz, CH_2Cl_2) of Poly(9-vinyl-carbazole-$(COCH_3)_2$) (PVKdac)

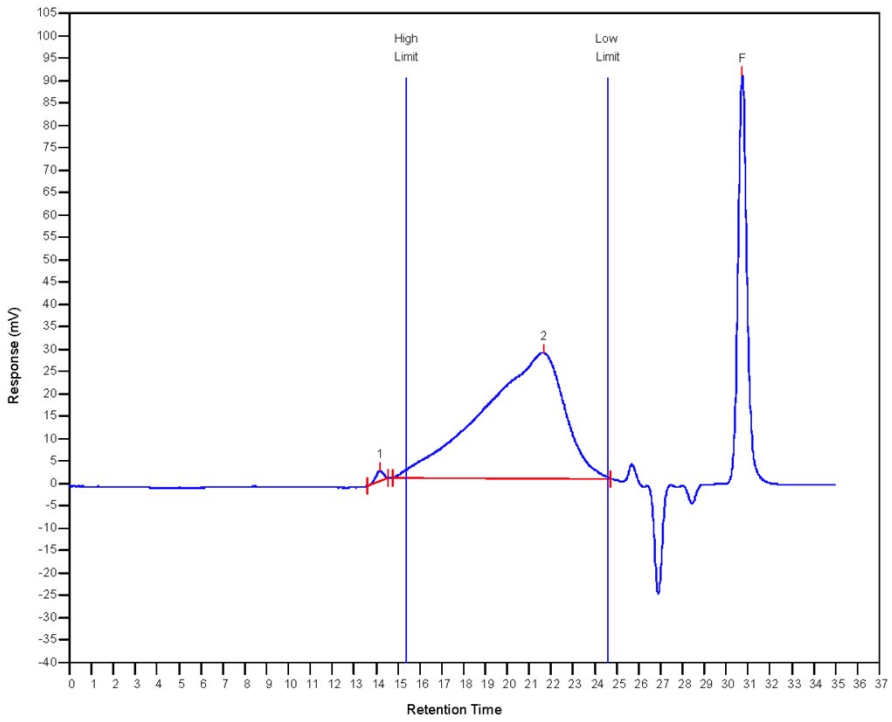

MW Averages

Peak No	Mp	Mn	Mw	Mz	Mz+1	Mv	PD
1	464893	460527	467825	475349	483057	466712	1.01585
2	6215	8382	20056	53944	103363	17168	2.39275
3	0	0	0	0	0	0	0

Figure 4: Results of the SEC analysis of PVKdac (eluent: DMF with 1 g/L LiBr, temperature : 80°C, flow rate : 0.80 ml/min, RI detector, PS calibration standards)

S2 TGA analysis of the SWCNT-NMP composite

This section shows the TGA results obtained for the p-SWCNT pellets after extensive acetone washing and drying. Figure 5 shows the TGA temperature (°C) and time (min) profile for the SWCNT-NMP composite. The different phases are identified using the FTIR analysis of the produced gas shown in Figure 6. The C-H stretching bond is observed throughout the experiment. From ~250°C, NMP starts to evaporate; then from ~400 °C, both NMP and methane (CH_4) signals are observed; which is consistent with a phase of both evaporation and combustion of NMP. From ~560 °C, no NMP signal is observed; the corresponding weight loss percentage, 28.6 %, is taken as the mass percentage of NMP in the pellet. Finally, above 780 °C, CO production is observed, indicating combustion of the SWCNT (allowed by small air leakage in the system). It is unclear whether CO_2 is produced above 780 °C, as the peak falls in the same range as the thermal stretching of the C-H bond.

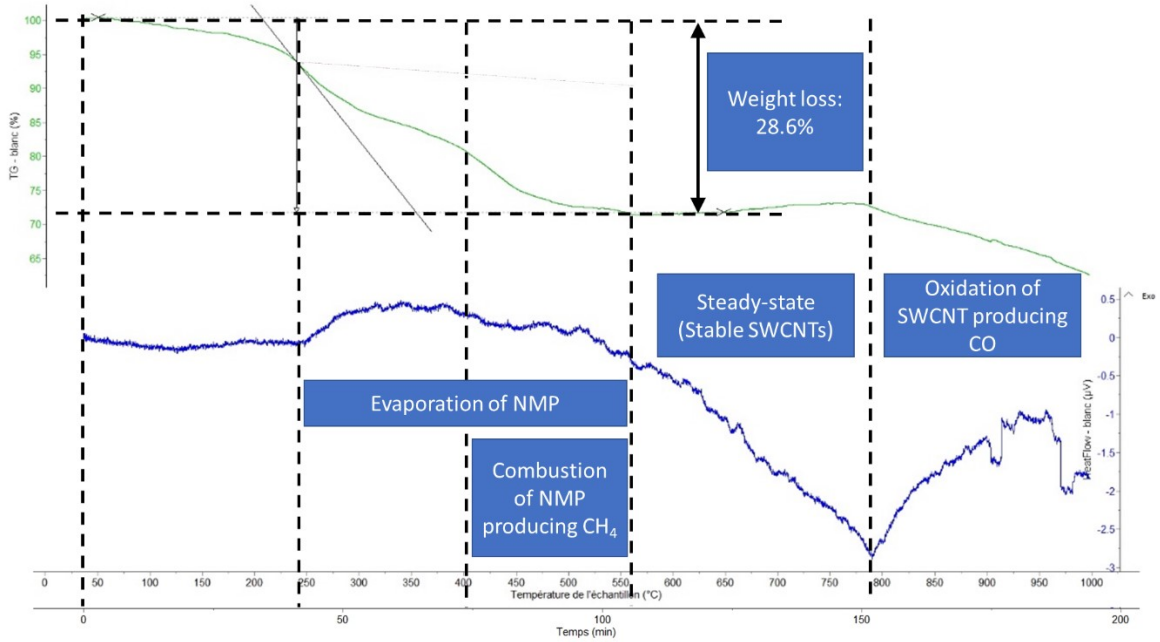

Figure 5: TGA temperature (°C) and time (min) profile of the SWCNT-NMP composite. Bottom – Heat flow as a function of temperature. Top – Weight loss (%) as a function of temperature.

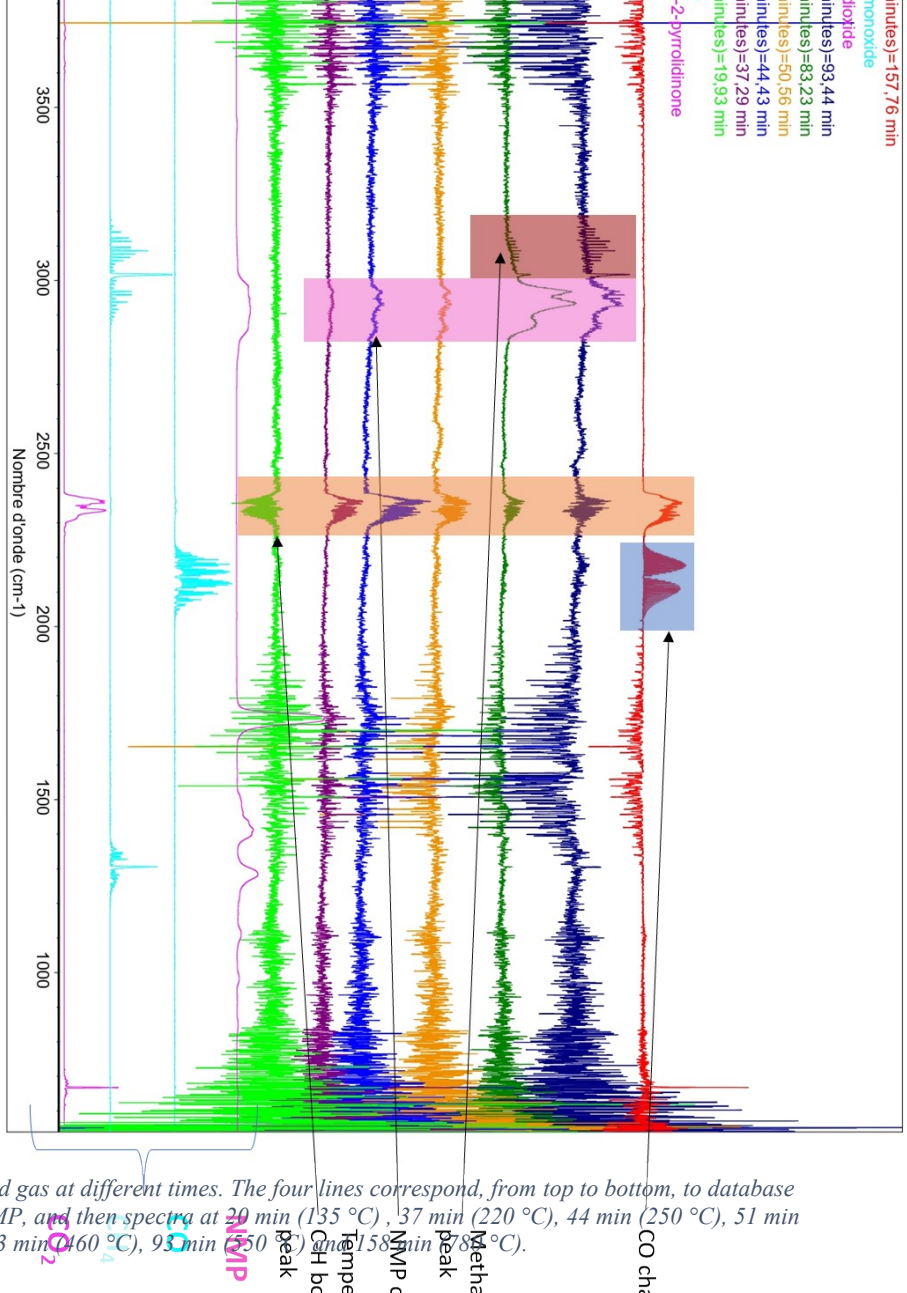

Figure 6: FTIR analysis of the produced gas at different times. The four lines correspond, from top to bottom, to database FTIR spectra for CO_2, CH_4, CO and NMP, and then spectra at 20 min (135 °C) , 37 min (220 °C), 44 min (250 °C), 51 min (285 °C), 83 min (460 °C), 93 min (550 °C) and 158 min (788 °C).

S3 AFM image analysis

Figure 7 shows 5 µm x 5 µm AFM height and phase images of a pristine SWCNT suspension and of PVT:SWCNT (0.86:1) and (1.7:1) dispersions after spin-coating on glass slides. In particular, they show the random organization of the SWCNTs after spin-coating and suggest an increased SWCNT diameter in the functionalized dispersions. Figure 8, Figure 9 and Figure 10 illustrate the process of SWCNT diameter analysis based on the 5 µm x 5 µm AFM height images of the three samples. Table 1, Table 2, and Table 3 show the diameters measured according to this process for the 3 different formulations. It is worth mentioning that the slight saturation effect visible on some of the height profiles (e.g., Figure 9(e) and (g)) is due to the limited number of pixels available along the profiles, which is a consequence of the image resolution. This is expected to lead to a slight underestimation of the diameters. Similarly, the background was flattened to better isolate the SWCNT shape. Processing was tested with and

without the background flattening, and it appears that flattening led to a slight underestimation of diameter by ~0.5 nm.

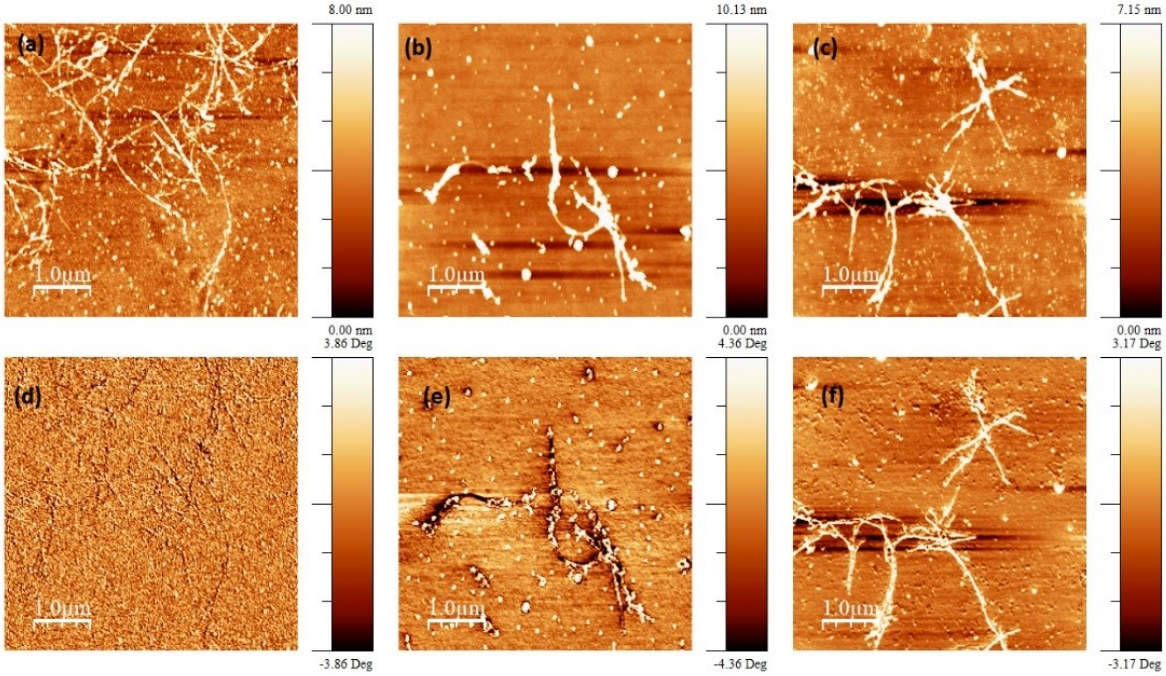

Figure 7: (5 µm x 5 µm) AFM height (top) and phase (bottom) images of spin-coated deposits made of (a,d) pristine SWCNT, (b,e) PVT:SWCNT (0.86:1), and (c,f) PVT:SWCNT (1.7:1)

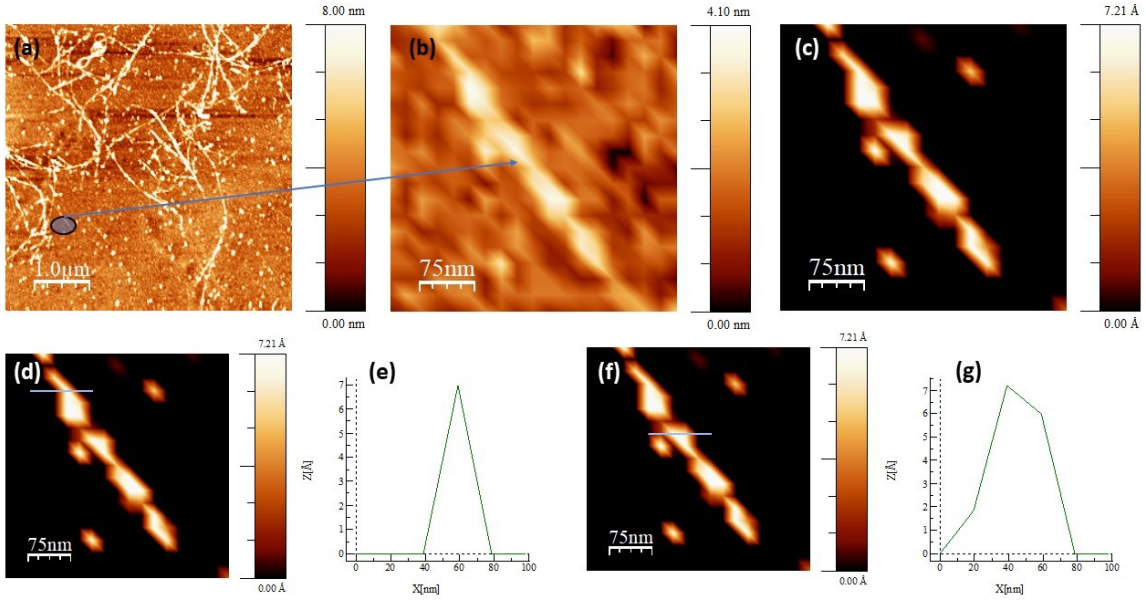

Figure 8: Analysis of an AFM (5 µm x 5 µm) height image of a spin-coated pristine SWCNT deposit to extract SWCNT diameters: a) original image; b) focus on an individual nanotube; c) removal of the background; d),e) height profile along a specific line; f),g) height profile along a second line.

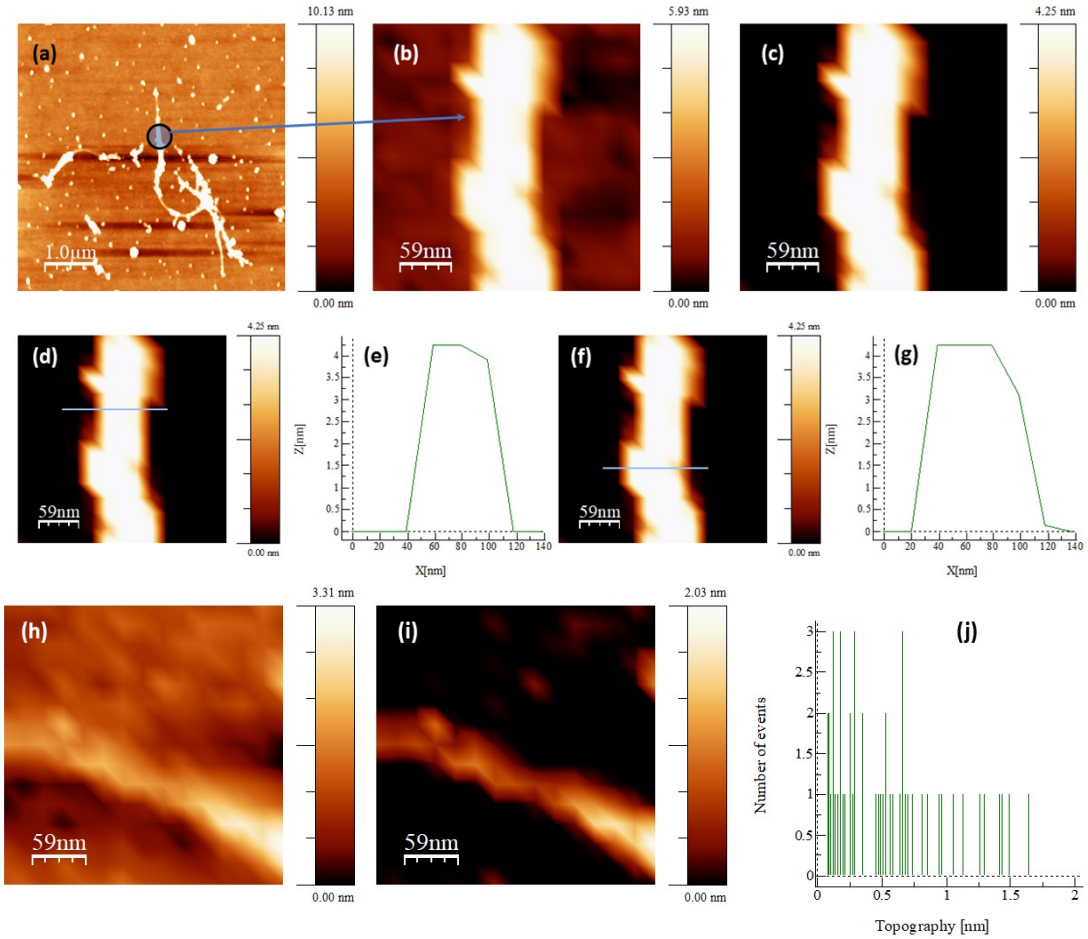

Figure 9: Analysis of an AFM (5 µm x 5 µm) height image of a spin-coated PVT: SWCNT (0.86:1) deposit to extract SWCNT diameters: a) original image; b) focus on an individual nanotube; c) removal of the background; d),e) height profile along a specific line; f),g) height profile along a second line; h) focus on a second nanotube in image a); i) removal of background from image; h) height distribution analysis the full nanotube.

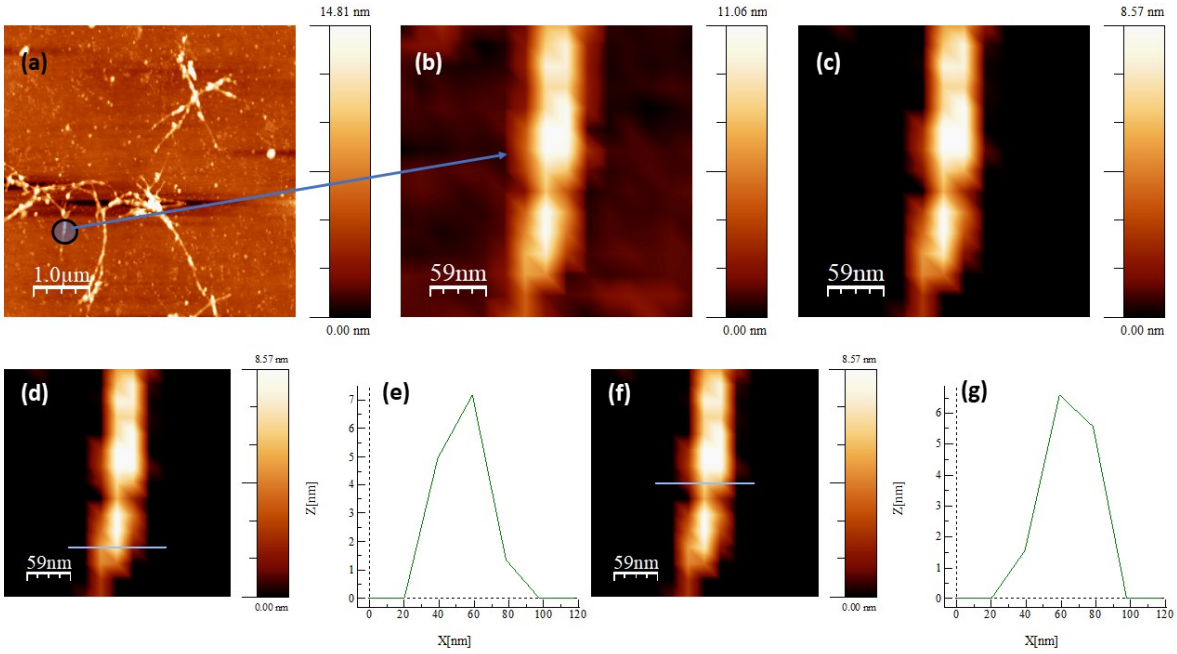

Figure 10: Analysis of an AFM (5 µm x 5 µm) height image of a spin-coated PVT: SWCNT (1.7:1) deposit to extract SWCNT diameters: a) original image; b) focus on an individual nanotube; c) removal of the background; d),e) height profile along a specific line; f),g) height profile along a second line.

Table 1: SWCNT diameters observed on the AFM images of the pristine SWCNT deposit

SWCNT	Tube 1	Tube 2	Tube 3
Place 1	0,6	0,6	0,8
Place 2	0,6	0,7	1,6
Place 3	0,6	0,7	0,9
Place 4		0,7	
Mean each tube	**0,6**	**0,7**	**1,1**
Mean	**0,79**		
Standard Deviation	**0,27**		

Table 2: SWCNT diameters observed on the AFM images of the PVT:SWCNT 0.86:1 deposit

PVT:SWCNT (0.86:1)	Tube 1	Tube 2	Tube 3	Tube 4
Place 1	4	4	4	4,5
Place 2	4	4	4	3,6
Place 3			9,5	7
Place 4			7	8,5
Place 5				5,5
Place 6				3,5
Mean each tube	4	4	6,1	5,4
Mean	**4,9**			
SD	**1,1**			

Table 3: SWCNT diameters observed on the AFM images of the PVT:SWCNT 1.7:1 deposit

PVT:SWCNT (1.7:1)	Tube 1	Tube 2	Tube 4
Place 1	4	8,5	5,5
Place 2	7,5	7	8
Place 3	4,5	6,5	8
Mean each tube	**5,3**	**7,3**	**7,2**
Overall mean	**6,6**		
SD	**1,1**		

S4 Time-resolved UV-Vis absorption curve for a pristine SWCNT ink

Figure 11 shows the UV-Vis absorbance of a pristine SWCNT suspension with a concentration of 4.8 ppm between 0 and 7000 s, with a zoom in on the steady-state part from 3000 s, on. The stock solution of SWCNTs was composed of 24 ppm, and a diluted solution of 4.8 ppm was obtained by diluting 500 µL of SWCNT ink in 2000 µL of NMP. The mean of the signal above 3000 s is 0.00089 and its standard deviation is 0.00036, resulting in a detection limit of the method of 0.0012 (3.2 times the standard deviation).

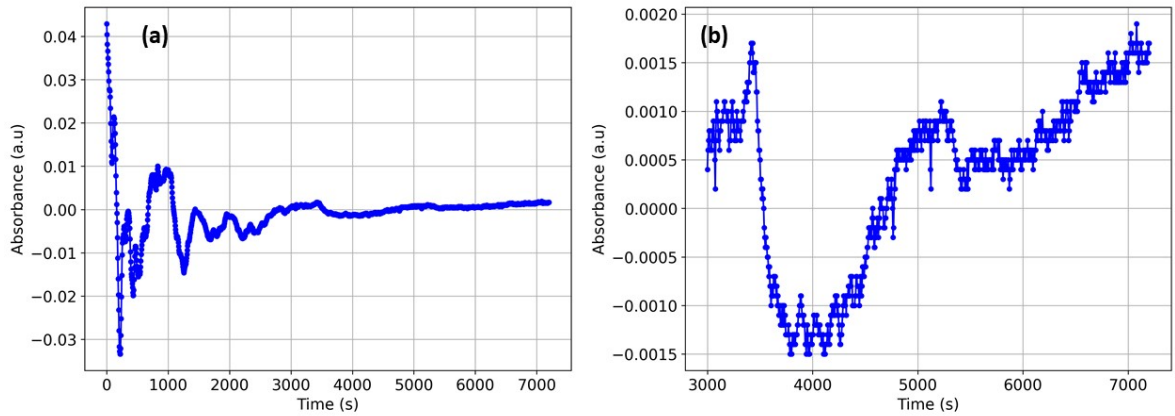

Figure 11: Time-resolved UV-VIs absorption of a pristine SWCNT suspension with a concentration of 4.8 ppm. Top: full spectrum. Bottom: focus on the 3000 to 7000 s portion used to calculated the standard deviation of the differential absorbance method.

S5 Raman spectroscopy of the pristine SWCNTs

Figure 12 shows the Raman spectrum of the pristine SWCNT suspension spin-coated on a soda-lime glass slide.

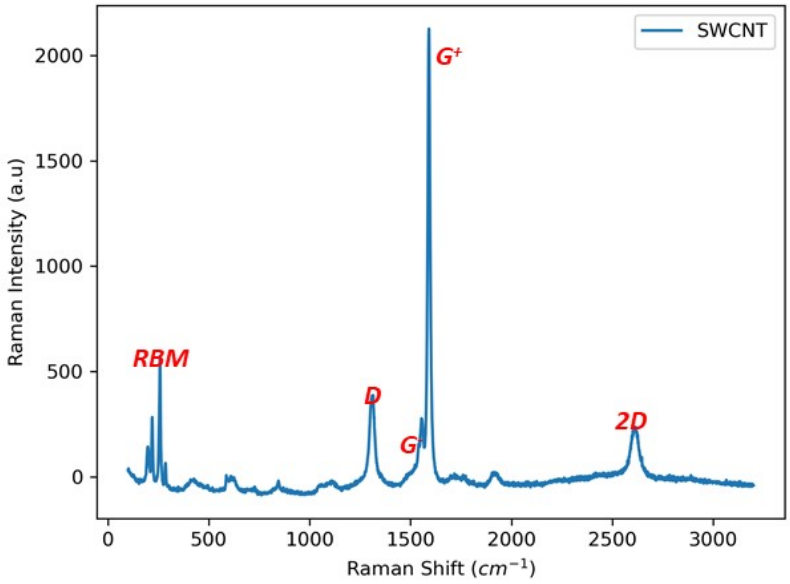

Figure 12: Raman spectrum of the pristine-SWCNT suspension spin-coated on a soda lime glass slide under 633 nm laser excitation

S6 Kinetics parameter for adsorption of PVT on SWCNT

Table 4 summarizes all the parameters found for the pseudo-second-order kinetic models for the various PVT:SWCNT stoichiometries. According to the PSO equation (1) $\frac{t}{q_t} = \frac{1}{k_2 {q_e}^2} + \left(\frac{1}{q_e}\right)t$, the variable t/q_t can be fitted by a linear equation $\frac{t}{q_t} = At + B$ with the slope $A = \frac{1}{q_e}$ and the y-intercept $B = \frac{1}{k_2 {q_e}^2}$. The coefficient R^2 is defined as the regression coefficient of the fit. One derives $q_e = \frac{1}{A}$ and $k_2 = \frac{A^2}{B}$. The associated uncertainties on q_e and k_2, dq_e and dk_2, are given by $dq_e = \frac{dA}{A^2}$ and $\frac{dk_2}{k_2} = 2\frac{dA}{A} + \frac{dB}{B}$, where dA and dB are the standard deviations on A and B, respectively. For $t \ll t_{th} = \frac{1}{k_2 q_{e2}}$, equation (1) is rewritten as $\frac{t}{q_t} \sim \frac{1}{k_2 {q_e}^2}$. In other words, q_t increases linearly with t and the corresponding slope is $q_0^{'} = k_2 {q_{e2}}^2$. Both the PSO-predicted and experimental values for $q_0^{'}$ and t_{th} are provided. For the stoichiometry 0.6:1, the PSO is verified from 50 s only.

Table 4: Kinetic parameters for adsorption of PVT on SWCNTs.

Stoichiometry PVT:SWCNT X:1	**0,6**	**1,4**	**2,1**	**4,4**	**6,7**	**8,4**	**10,6**	**12,2**	**13,6**	**15,6**
Initial PVT concentration (ppm)	2,3	5,4	7,9	16,9	25,5	32,1	40,3	46,4	52,0	59,5
R^2	0,938	0,969	0,998	1,000	0,999	0,995	0,999	0,999	1,000	0,990
A (slope) (g/mg)	2,2E-3	6,1E-4	5,9E-4	2,5E-4	1,9E-4	1,9E-4	1,7E-4	1,6E-4	1,5E-4	1,4E-4
B (y-intercept) (s.g/mg)	1,3E-1	4,4E-2	4,5E-2	1,8E-2	3,6E-2	6,3E-2	2,6E-2	9,9E-2	4,5E-2	1,0E-1
dA (uncertainty on A)	1,9E-5	3,6E-6	7,2E-7	1,7E-7	2,7E-7	4,2E-7	1,3E-7	1,8E-7	9,4E-8	4,2E-7
dB (uncertainty on B)	1,0E-2	1,9E-3	2,3E-3	5,3E-4	3,9E-4	1,3E-3	4,0E-4	5,6E-4	2,9E-4	1,3E-3
q_e (mg/g)	460	1 649	1 706	3 990	5 278	5 357	6 037	6 334	6 650	7 314
k_2 (g/mg.s)	3,7E-5	8,4E-6	7,7E-6	3,5E-6	9,9E-7	5,5E-7	1,1E-6	2,5E-7	5,1E-7	1,8E-7
dq_e/qe (in %)	0,88	0,60	0,12	0,07	0,14	0,22	0,08	0,11	0,06	0,31
dk_2/k_2 (in %)	9,9	5,5	5,3	3,1	1,3	2,5	1,7	0,8	0,8	1,9
dq_e	4,1	9,9	2,1	2,7	7,5	12,0	4,7	7,2	4,1	22,4
dk_2	3,7E-6	4,7E-7	4,0E-7	1,1E-7	1,3E-8	1,4E-8	1,8E-8	2,0E-9	4,0E-9	3,4E-9
Predicted linearity range (s) $t \ll t_{th}$	59	72	77	71	191	339	155	626	296	754

linearity range observed (s)	N/A	60	40	35	45	35	35	35	100	100
initial slope predicted q_0' (mg/(g.s))	7,9	23	22	56	28	16	39	10	22	10
initial slope q_0' measured (mg/g/s)	N/A	14	23	34	30	22	33	36	10	11

S7 Isotherm modeling – Description of the different models

In this section, q_e designates the equilibrium adsorption capacity (mg/g) and C_e the initial PVT concentration (*mg/L*). The model formulations and descriptions are based on [1]**.**

S7.1 Two-parameter models

S7.1.1 Langmuir isotherm

The Langmuir isotherm is mostly used to describe monolayer adsorption on homogeneous surfaces with nonspecific adsorption sites within the adsorbent. It is formulated as $q_e = \frac{K_L C_e}{1 + a_L C_e}$ where K_L and a_L are the two model parameters. The former is related to the adsorption capacity of each binding site, the latter to the adsorption energy. The high concentration limit in the Langmuir model is expressed by: $q_m(mg/g) = \frac{K_L}{a_L}$, also called the maximum adsorption capacity.

S7.1.2 Freundlich isotherm

The Freundlich isotherm is an empirical model expressed as $q_e = K_f C_e^{1/n}$, where K_f and n are the two empirical model parameters [1]. It can be used to model processes with a heterogeneous adsorption surface and can also account for multilayer adsorption.

S7.1.3 Temkin isotherm

The Temkin isotherm assumes that the energy of adsorption varies linearly with surface area and that adsorption is characterized by a uniform distribution of binding energies up to some maximum binding energy. The Temkin isotherm is expressed by $q_e = \frac{RT}{b} \ln (K_{Te} C_e)$, where K_{Te} is the equilibrium binding constant (L/g), b is related to the heat of adsorption (J/mol), R is the gas constant (8.3×10^{-3} kJ/K mol) and T is the absolute temperature (K).

S7.1.4 Dubinin–Radushkevich isotherm

The Dubinin-Radushkevich isotherm model is used to model the adsorption mechanism on a heterogeneous surface, distinguishing between physical and chemical adsorption processes. The Dubinin–Radushkevich model is expressed as $q_e = q_m \exp \frac{(RT\ln(1 + 1/C_e))^2}{-2E^2}$

where q_m is again the maximum adsorption capacity (mg/g) and E is the energy of adsorption (kJ/mol). If E < 8 kJ/mol, the adsorption process is considered to be physical adsorption (physisorption). If E > 8 kJ/mol, the process is considered to be chemical adsorption (chemisorption).

S7.2 Three-parameter models

S7.2.1 Redlich–Peterson isotherm

At low adsorbate concentrations, the Redlich-Peterson isotherm approximates Henry's law, where adsorption is directly proportional to adsorbate concentration. At high concentrations it behaves like the Freundlich isotherm, taking into account the heterogeneity of the adsorbent surface. It is given by $q_e = \frac{K_R C_e}{1 + \alpha_R C_e^{\beta}}$, where K_R (L/g) and α_R (L/mg) are the Redlich–Peterson isotherm constants. The coefficient α_R relates to the adsorption energy and the coefficient β is an exponent between 0 and 1. When β is close to 1, the Redlich–Peterson isotherm simplifies to the Langmuir isotherm, suggesting a more homogeneous surface, and β less than 1 indicates a heterogeneous surface.

S7.2.2 Sips isotherm

The Sips isotherm model equation is derived from the Langmuir and Freundlich isotherms. It assumes that the adsorption occurs on heterogeneous surfaces with energetically nonuniform adsorption sites. The model incorporates both monolayer and multilayer adsorption processes. The model can be written as $q_e = \frac{q_m a_s C_e^{1/n}}{1 + a_s C_e^{1/n}}$ where q_m is the maximum adsorption capacity (mg/g) and a_s is the Sips constant related to the energy of adsorption. The parameter n allows to account for a range of adsorption site energies. When n is close to 1, there is only a single type of adsorption site, when it is greater than 1, there are multiple types of adsorption sites.

S7.2.3 Toth isotherm

The Toth isotherm model is also an empirical equation that combines features of the Langmuir and Freundlich isotherms. It is suitable for describing adsorption on heterogeneous surfaces with multiple layers. The Toth model assumes that there is an interaction between adsorbed molecules that affects the adsorption process. It introduces a parameter *n* which takes into account the heterogeneity of the surface. It is expressed as $q_e = \frac{q_m C_e}{(K_{T0} + C_e^n)^{1/n}}$. For *n* = 1 this isotherm reduces to the Langmuir equation.

S7.3 High and low concentration limits and linearization of the models

To understand the similarities and differences between the models, it is particularly useful to linearize them in the high and low concentration limits, and to derive their high concentration limit. This information is summarized in Table 5. Very briefly, for $n = 1$ and $\beta = 1$, Langmuir, Toth, Sips and Redlich Peterson are equivalent. The only difference – mathematically – between the Redlich Peterson and Sips models is the fact that in the latter *n* is an integer, so *1/n* takes only a discrete set of values between 0 and 1, while in the former β takes continuous values between 0 and 1. Sips and Toth differ mainly in the speed with which q_m is reached, with Toth having a sharper initial slope and then a smaller final slope (quasy-steady state). The Temkin model is similar to the Langmuir model at low concentration (linear increase), but has no high concentration limit. It continues to increase logarithmically with increasing concentration. Similarly, Freundlich is similar to Sips at low concentration but has no high concentration limit. Finally, the Dubinin–Radushkevich model behaves as as special case of the Toth model for n=2 at high concentration, but rises much faster than Toth at low concentration.

Table 5: Comparison of limit behaviors of the models

Model	***Low concentration limit***		***High concentration limit***		
	Threshold	*Linearized expression*	Threshold	*Linearized expression*	*Limit*
Sips $q_e = \frac{q_m a_s C_e^{1/n}}{1 + a_s C_e^{1/n}}$	$C_e \ll \frac{1}{a_s^n}$	$q_e = q_m a_s C_e^{1/n}$	$C_e \gg \frac{1}{a_s^n}$	$q_e = q_m(1 - \frac{1}{a_s C_e^{1/n}})$	q_m
Toth $q_e = \frac{q_m C_e}{(K_{T0} + C_e^n)^{1/n}}$	$C_e \ll \frac{1}{K_{T0}^{1/n}}$	$q_e = \frac{q_m C_e}{K_{T0}}$	$C_e \ll \frac{1}{K_{T0}^{1/n}}$	$q_e = q_m(1 - \frac{1}{n}\frac{K_{T0}}{C_e^n})$	q_m

Langmuir $q_e = \frac{q_m a_L C_e}{1 + a_L C_e}$	$C_e \ll \frac{1}{a_L}$	$q_e = q_m a_L C_e$	$C_e \gg \frac{1}{a_L}$	$q_e = q_m(1 - \frac{1}{a_L C_e})$	q_m
Redlich–Peterson $q_e = \frac{K_R C_e}{1 + \alpha_R C_e^{\beta}}$	$C_e \ll \frac{1}{a_R^{1/\beta}}$	$q_e = K_R C_e$	$C_e \gg \frac{1}{a_R^{1/\beta}}$	$q_e = \frac{K_R}{\alpha_R} C_e^{1-\beta}$	N/A
Temkin $q_e = \frac{RT}{b} \ln(K_{Te} C_e)$	$C_e \sim \frac{1}{K_{Te}} + \varepsilon$ $0 < \varepsilon \ll 1$	$q_e = \frac{RT}{b}\varepsilon$	N/A	N/A	N/A
Freundlich $q_e = K_f C_e^{1/n}$	$C_e \ll \frac{1}{K_f^n}$	$q_e = K_f C_e^{1/n}$	N/A	N/A	N/A
Dubinin–Radushkevich $q_e = q_m \exp\frac{(RT\ln(1 + 1/C_e))^2}{-2E^2}$	$C_e \ll 1$	$q_e = q_m \exp\frac{(RT\ln(C_e))^2}{2E^2}$	$C_e \gg 1$	$q_e = q_m(1 - \frac{(RT)^2}{2E^2 C_e^2})$	q_m

S8 Isotherm modelling – Selection of the optimal isotherm model for the pseudo-second order kinetics data of PVT

This section details the procedure implemented to fit all of the (C_e,q_e) pairs found for the various PVT:SWCNT stoichiometries with any of the models listed in the previous section, and to choose the one with the best metrics. The metrics used for the model selection were the nonlinear correlation coefficient *(R^2),* the mean absolute percentage error *(MAPE)* and the mean absolute error *(MAE)*, classically defined as $R^2 = \frac{1}{N}\sum_{i=1}^{N}({q_{cal}}^{i} - < q_{cal} >)({q_{exp}}^{i} - < q_{exp} >) \times \frac{1}{\sigma_{q_{cal}}\sigma_{q_{exp}}}$,

$MAPE = \frac{1}{N}\sum_{i=1}^{N}\frac{{q_{cal}}^{i} - {q_{exp}}^{i}}{{q_{exp}}^{i}} \times 100$, and $MAE = \frac{1}{N}\sum_{i=1}^{N}\left|{q_{cal}}^{i} - {q_{exp}}^{i}\right|$, where ${q_{exp}}^{i}$ and ${q_{cal}}^{i}$ are the experimentally derived and model calculated equilibrium adsorption capacities, respectively, for each stoichiometry *I*, and $< X >$ and σ_X are the mean and standard deviation, respectively, of the variable X. Other metrics (such as RMSE) are available in the literature and were tested. Since they yielded the same results, they are not reported here. The fitting procedure was performed using the *curve_fit* function of the *scipy* package in *Python 3*.

Importantly, the values of (C_e,q_e) have significant uncertainties, so this was taken into account in the fitting procedures: the estimation errors were classically assumed to be Gaussian, and random errors dC_e and dq_e were generated based on the experimental uncertainties and added to each value of C_e and q_e, respectively. For C_e, the relative uncertainty $\frac{\Delta C_e}{C_e}$ was approximated to the relative uncertainty of the molar absorption coefficient (7.6 % for this data set). For q_e, the uncertainty Δq_e was approximated to the sum of the uncertainty associated with the molar absorption coefficient (7.6 % relative uncertainty) and the uncertainty derived from the pseudo-second-order model (as reported in Table 4), yielding an average uncertainty of 346 mg/g ± 53%.

The fitting procedure was applied to the pairs $(C_e + dC_e, q_e + dq_e)$. This procedure was repeated 500 times, and the statistics (mean, standard deviation and coefficient of variation) of each derived metrics and fitting parameter were calculated. The means values are summarized in Table 6, while the coefficients of variation are reported in Table 7. Using this approach, the

best fitting model is the one with the highest R^2, lowest MAPE and MAE, and lowest coefficients of variation. If two models have a metric within three times the standard deviation of each other, they effectively have the same metric. A model that has one or more abnormally high coefficients of variation, even with the best metrics, is an unlikely model, because it means that the predictive ability of the model is low when measurement uncertainties are taken into account.

According to this interpretation, among the 7 models, this excludes the Toth and the RP models, since they each have an abnormal coefficient of variation on one of their model parameters; it also excludes the DR model, which has a significantly lower R^2 coefficient and higher MAE and MAPE. From the point of view of the R^2, MAE and MAPE metrics, Langmuir, Sips, Freundlich and Temkin are all equivalent models, with Sips being in practice equivalent to Langmuir here as it yields n~1.02. The Freundlich model has coefficients of variation similar to Temkin (6% on average over the two model parameters), and three times lower than Langmuir (18% on average). This suggests that either the Freundlich or Temkin models is more likely in this instance.

Table 6: Mean of the metrics and output parameters of each model, sorted from highest to lowest R^2. The most likely models are Langmuir, Temkin or Freundlich.

Model	***Name of the parameter***	***Isotherm Parameters***	***R^2***	*MAPE*	***MAE (mg/g)***
Toth $q_e = \frac{q_m C_e}{(K_{T0} + C_e^n)^{1/n}}$	q_m *(mg/g)*	9420	0.97	12 %	338
	K_{To} *(ppm^n)*	456			
	n	1.58			
Langmuir $q_e = \frac{q_m a_L C_e}{1 + a_L C_e}$	q_m *(mg/g)*	11200	0.96	15 %	351
	a_L *(ppm)*	0.0316			
Freundlich $q_e = K_f C_e^{1/n}$	K_f *(mg/g.ppm$^{-1/n}$)*	667	0.96	23 %	376
	n	1.69			
Redlich–Peterson $q_e = \frac{K_R C_e}{1 + \alpha_R C_e^{\beta}}$	K_R *(L/g)*	357	0.96	15%	367
	a_R *(ppm^{-b})*	0.0415			
	β	0.970			
	$q_m = \frac{K_R}{\alpha_R}$ *(mg/g)*	8600			
Sips $q_e = \frac{q_m a_s C_e^{1/n}}{1 + a_s C_e^{1/n}}$	q_m *(mg/g)*	12000	0.96	14 %	371
	a_s *(ppm$^{-1/n}$)*	0.0312			
	n	1.02			
Temkin $q_e = \frac{RT}{b} \ln (K_{Te} C_e)$	K_{Te} *(ppm^{-1})*	0.407	0.95	23 %	428
	RT/b (mg g^{-1})	2166			
Dubinin–Radushkevich	q_m *(mg/g)*	6256.1	0.91	26 %	575

	E (kJ/mol)	3.6
$q_e = q_m \exp \frac{(RT \ln (1 + 1/C_e))^2}{-2E^2}$		

Table 7: Coefficients of variation (all expressed in %) of the metrics and output parameters of each model, sorted from highest to lowest R². The most likely models are Langmuir, Temkin or Freundlich.

Model	***Name of the parameter***	***Isotherm Parameters***	***R^2***	*MAPE*	***MAE (mg/g)***
Toth $q_e = \frac{q_m C_e}{(K_{T0} + C_e^n)^{1/n}}$	q_m	28	1.8	25	27
	K_{To}	92			
	N	30			
Langmuir $q_e = \frac{q_m a_L C_e}{1 + a_L C_e}$	q_m	13	1.8	24	25
	a_L	23			
Freundlich $q_e = K_f C_e^{1/n}$	K_f	8.0	0.92	12	14
	n	4.0			
Redlich–Peterson $q_e = \frac{K_R C_e}{1 + \alpha_R C_e^{\beta}}$	K_R	11	2.0	23	25
	a_R	77			
	β	8.2			
Sips $q_e = \frac{q_m a_s C_e^{1/n}}{1 + a_s C_e^{1/n}}$	q_m	31	2.0	15	22
	a_s	25			
	n	5.7			
Temkin $q_e = \frac{RT}{b} \ln (K_{Te} C_e)$	K_{Te}	7.9	1.9	8.3	19
	RT/b	5.1			
Dubinin–Radushkevich $q_e = q_m \exp \frac{(RT \ln (1 + 1/C_e))^2}{-2E^2}$	q_m	5.1	3.0	12	17
	E	36			

S9 Adsorption capacity of PVT on SWCNT for different SWCNT concentrations

Table 8 shows the adsorption capacity as a function of the initial PVT concentration for different SWCNT concentrations. The concentration of SWCNT 3.8 ppm gathers the data reported in the previous sections. The other concentrations were tested approximately 1 year after the 3.8 ppm concentration, using the same batch of SWCNT powder.

Writing C_e=X C_{CNT}, all the isotherm models, except for DR, are rewritten as a function of X and the fitting procedures detailed in the previous section are used again. DR is excluded as its formulation cannot be independent of C_{CNT}. Even in the absence of uncertainty, the fitting procedure for the Toth and Sips models does not converge. The metrics of the remaining models are shown in Table 9.

Table 8: Adsorption capacity for different SWCNT concentration (left column)

SWCNT concentration (ppm)											
	0,74	PVT:CNT stoichiometry (X:1)	5	10	20	30					
	0,74	PVT initial concentration (ppm)	3,71	7,41	14,83	22,24					
	0,74	Adsorption capacity (g/g)	4,66	9,11	15,00	17,92					
	1,5	PVT:CNT stoichiometry (X:1)	5	10	20						
	1,5	PVT initial concentration (ppm)	7,41	14,83	29,66						
	1,5	Adsorption capacity (g/g)	4,32	5,72	12,13						
	3,8	PVT:CNT stoichiometry (X:1)	0,6	1,4	2,1	4,4	6,7	8,4	10,6	12,2	13,6	15,6
	3,8	PVT initial concentration (ppm)	2,33	5,44	7,92	16,91	25,47	32,14	40,30	46,42	52,00	59,52
	3,8	Adsorption capacity (g/g)	0,46	1,65	1,71	3,99	5,28	5,36	6,04	6,33	6,65	7,31
	4,0	PVT:CNT stoichiometry (X:1)	0,5	1	2	5					
	4,0	PVT initial concentration (ppm)	1,97	3,95	7,90	19,77					
	4,0	Adsorption capacity (g/g)	0,42	0,84	1,76	3,84					
	8,5	PVT:CNT stoichiometry (X:1)	0,2	0,5	1	2	3,5	5			
	8,5	PVT initial concentration (ppm)	1,69	4,23	8,46	16,95	29,66	42,37			
	8,5	Adsorption capacity (g/g)	0,20	0,50	1,00	1,82	3,08	4,35			

Table 9: Mean of the metrics and output parameters of each model, with uncertainty (in %).

Model	***Name of the parameter***	***Isotherm Parameters***	***R^2***	*MAPE*	***MAE (g/g)***
Langmuir $q_e = \frac{q_m a_L C_{CNT} X}{1 + a_L C_{CNT} X}$	q_m *(g/g)*	230 ± 180 %	0.92 ± 1.6%	20 % ± 12 %	0.86 ± 9.5 %
	$q_m a_L C_{CNT}$ *(ppm.g/g)*	0.71 ± 6.0%			
	$a_L C_{CNT}$ *(ppm)*	0.0071 ± 31 %			
Freundlich $q_e = K_f C_{CNT}^{1/n} X^{1/n}$	$K_f C_{CNT}^{1/n}$ *(g/g.ppm$^{-1/n}$)*	0.91 ± 10 %	0.93 ± 1.6 %	17 %± 12 %	0.78± 11 %
	n	1.2 ± 5.0 %			
Redlich–Peterson $q_e = \frac{K_R C_{CNT} X}{1 + \alpha_R C_{CNT}^{\beta} X^{\beta}}$	$K_R C_{CNT}$ *(L/g)*	5200 ± 60 %	0.93 ± 1.7 %	16% ± 12 %	0.76 ± 11 %
	$\alpha_R C_{CNT}^{\beta}$ *(ppm^{-b})*	5600 ± 57 %			
	β	0.13 ± 34 %			

S10 Adsorption kinetics and isotherm modelling for PVKdac

Figure 13 shows the time-resolved absorption spectra of PVKdac:SWCNT 10.8:1 with two peaks at 295 nm and 367 nm. Figure 14 shows the quantity t/q_t as a function of time t over the linear range, confirming the pseudo-second order kinetics. Figure 15 shows the equilibrium capacity q_{e2} derived from the PSO and the final adsorption capacity q_{final} as a function of the stoichiometry, the latter being on average 80% smaller than the former as shown in Figure 16). The initial gradient of qt (dqt/dt(t=0)) and the second order rate constant k_2 are displayed in Figure 17 and Figure 18, respectively. All the relevant kinetic coefficients for PVKdac are assembled in Table 10. Finally, the relationship q_t as a function of the concentration is fitted by the different isotherm models as described in the previous section. The resulting acceptable models are summarized in Table 11.

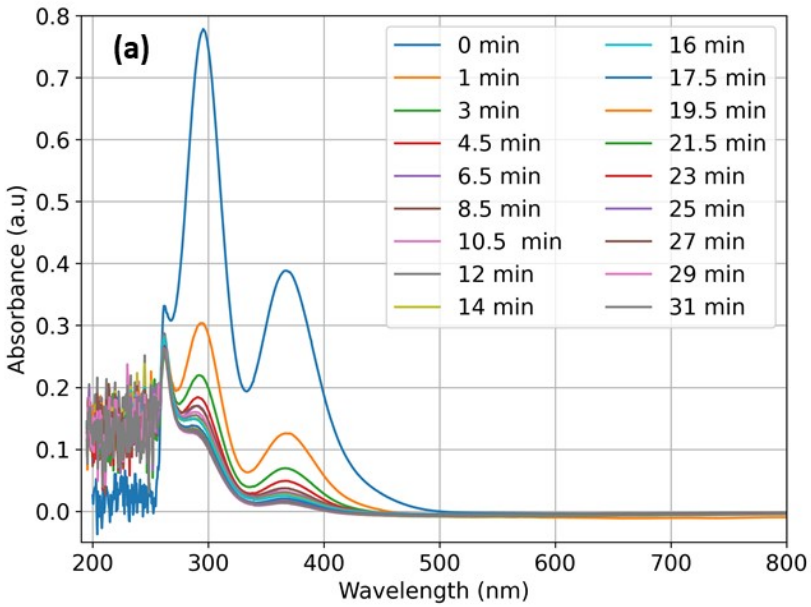

Figure 13: Time-resolved UV-Vis absorption spectra for the stoichiometry of PVKdac:SWCNT (10.8:1).

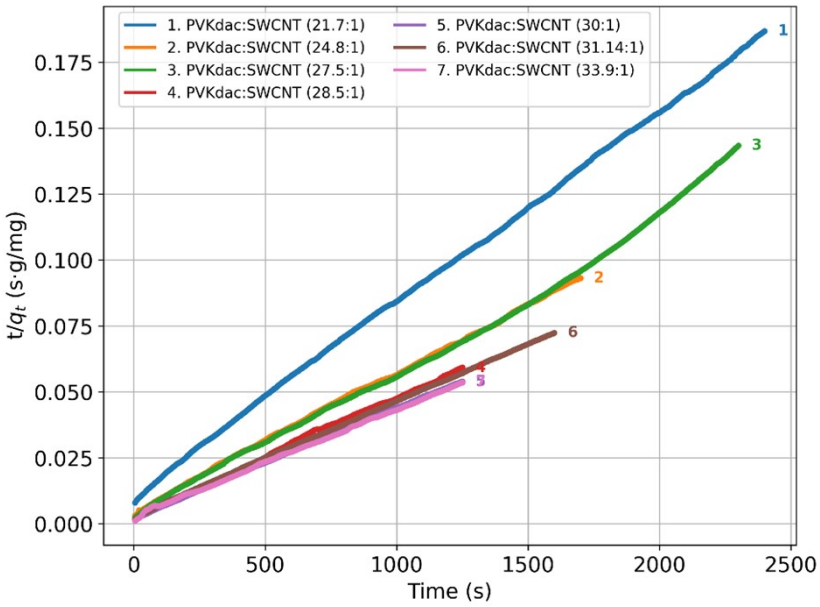

Figure 14: Quantity t/qt plotted as a function of t, for different PVKdac:SWCNT stoichiometry. Only the linear range for each stoichiometry is displayed here

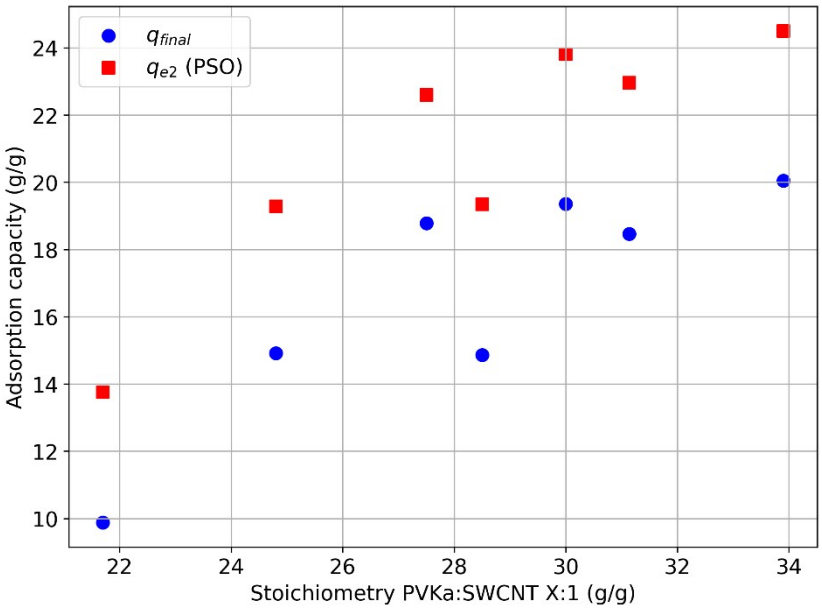

Figure 15: Equilibrium adsorption capacity qe_2 (derived from the pseudo second order kinetics) and final adsorption capacity q_{final} (average of q_t over the last 50 s of the kinetics) as a function of PVKdac:SWCNT stoichiometry.

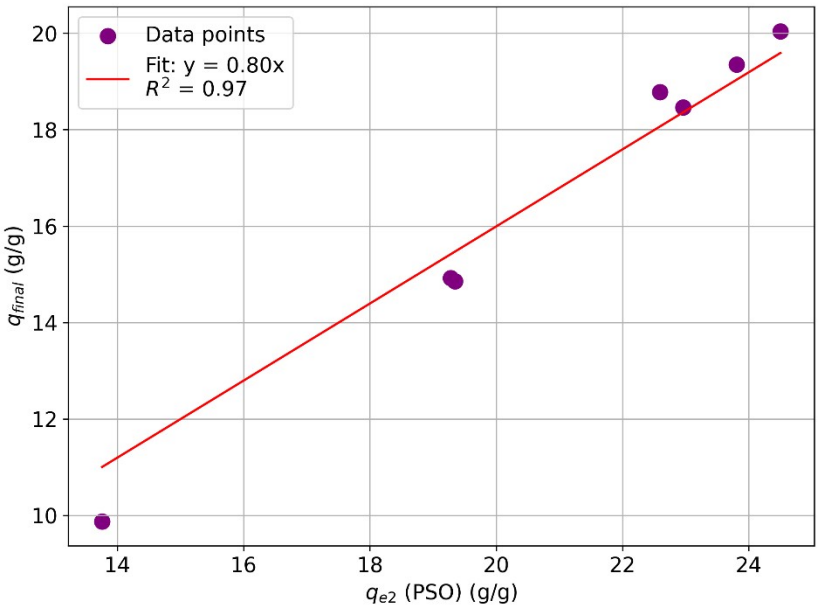

*

Figure 16: Linear trend between the equilibrium adsorption capacity qe_2 and the final adsorption capacity q_{final}.

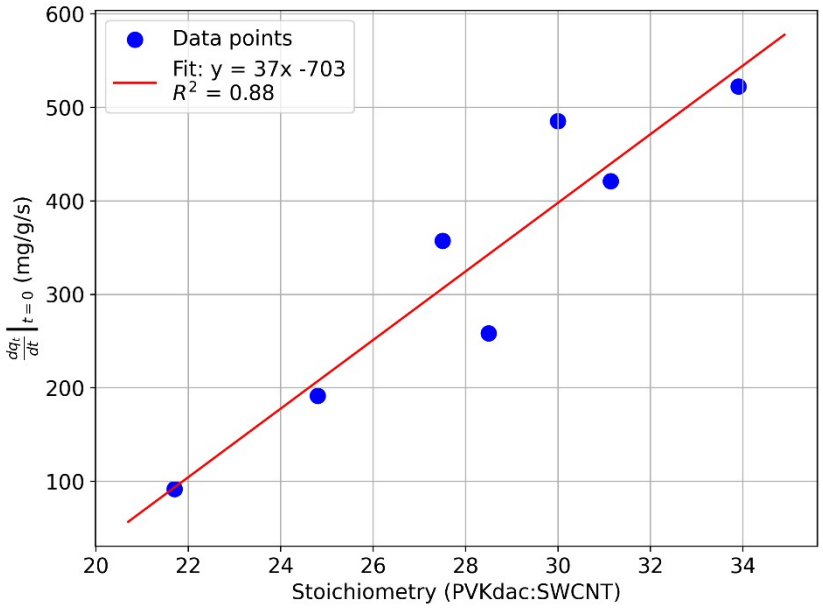

Figure 17: Initial slope $dq_t/dt(t=0)$ derived from the linear fit of q_t over the first 20 to 40 s of the kinetics

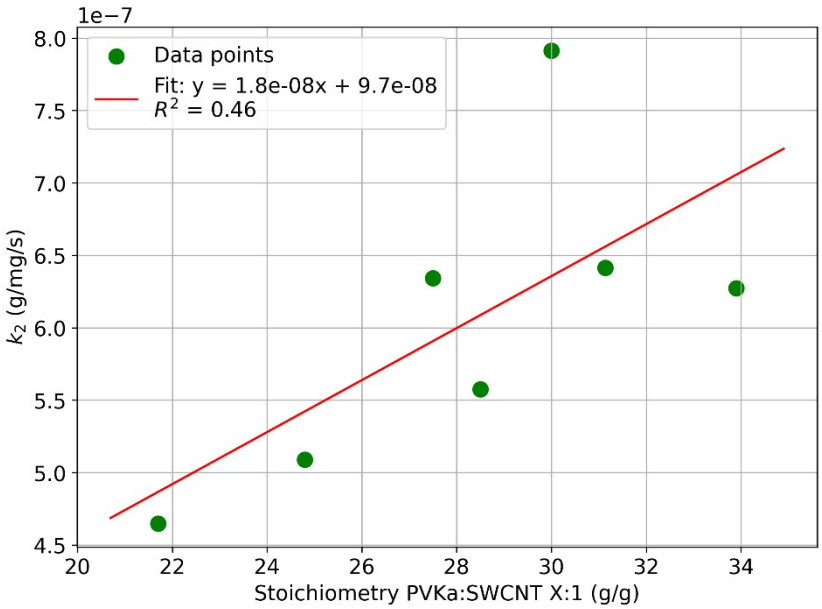

Figure 18: Pseudo-second order rate constant k_2 derived from the linear fit of t/q_t, as a function of the stoichiometry.

Table 10: Kinetic parameters for adsorption of PVKdac on SWCNTs. R^2 is the correlation coefficient for the linear fit of t/qt as a function t; q_{final} and dq_{final} are respectively the average and the standard deviation of qt over the last 50s of the kinetics experiment; q_{e2} and k_2, and the corresponding uncertainties dq_{e2} and k_2, are derived from the linear fit of t/q_t. The initial gradient $dq_t/dt(t=0)$ is derived by linear fit of qt as a function of t over the initial 20 s to 40 s of the kinetics.

Stoichiometry PVKdac:SWCNT X:1	21,7	24,8	28,5	27,5	30	31,14	33,9
Initial PVKdac concentration (ppm)	69	79	90	87	95	99	108
R^2	1,000	0,999	0,999	0,999	0,999	1,000	1,000
q_{final} (mg/g)	9880	14900	14900	18800	19400	18500	20000
dq_{final}/q_{final} (%)	0,47%	0,28%	0,33%	0,45%	0,33%	0,37%	0,18%
q_{e2} (mg/g)	13800	19300	19300	22600	23800	23000	24500
k_2 (g/mg.s)	4,6E-7	5,1E-7	5,6E-7	6,3E-7	7,9E-7	6,4E-7	6,3E-7
dq_{e2}/qe_2 (in %)	0,08	0,14	0,21	0,12	0,18	0,08	0,10
dk_2/k_2 (in %)	0,92	1,70	2,17	2,49	2,92	1,20	1,65
initial gradient dqt/dt(t=0) (mg/g/s)	92	191	258	357	485	421	522

Table 11: Fitting of $q_e=q_{final}$ as a function of the initial PVKdac concentration C_e by different isotherm models, accounting for the uncertainties on q_{final} and C_e. Only the models with moderate (<<100 %) coefficient of variations are listed.

Model	***Name of the***	***Isotherm***	***R^2***	*MAPE*	***MAE***

	parameter	***Parameters***			***(g/g)***
Langmuir linearized $q_e = q_m(1 - \frac{1}{a_L C_e})$	*q_m (g/g)*	37 ± 7.9 %	0.76 ± 12 %	8.4 % ± 25 %	1.3± 22%
	a_L (ppm)	0.021 ± 6.2 %			
Dubinin–Radushkevich $q_e = q_m \exp\ -\ \frac{(RT\ln(1 + 1/C_e))^2}{2E^2}$	*q_m (mg/g)*	31 ± 9.2 %	0.75 ± 13 %	8.8 % ± 24 %	1.4 ± 23 %
	E (kJ/mol)	4900 ± 15 %			
Dubinin–Radushkevich linearized $q_e = q_m(1 - \frac{(RT)^2\ 1}{2E^2\ C_e{}^2})$	*q_m (g/g)*	27 ± 5.6 %	0.77 ± 13 %	8.1 % ± 28 %	1.3 ± 26 %
	E (kJ/mol/ppm)	2800 ± 9.5 %			
Temkin $q_e = \frac{RT}{b}\ln(K_{Te} C_e)$	*K_{Te} (ppm^{-1})*	0.026 ± 12 %	0.74 ± 13 %	9.3 % ± 23 %	1.4 ± 21 %
	RT/b (g/g)	21 ± 16 %			
Freundlich $q_e = K_f C_e^{1/n}$	*K_f (g/g.ppm$^{-1/n}$)*	0.19 ± 17 %	0.66 ± 13 %	11 % ± 16 %	1.6 ± 17 %
	n	1.0± 3.3 %			

S11 Adsorption kinetics and isotherm modelling for PVIm

Figure 20 shows the time-resolved absorption spectra of PVIm:SWCNT 7:1 with two peaks at 295 nm and 367 nm. Figure 20 shows the quantity t/q_t as a function of time t over the linear range, confirming the pseudo-second order kinetics. Figure 21 shows the equilibrium capacity q_{e2} derived from the PSO and the final adsorption capacity q_{final} as a function of the stoichiometry, the latter being on average 74% smaller than the former (see Figure 22). The initial gradient of q_t ($dq_t/dt(t=0)$) and the second order rate constant k_2 show no trend as a function of stoichiometry and are therefore not displayed here. All the relevant kinetic coefficients for PVIm are assembled in Table 12. Finally, the relationship q_t as a function of concentration is fitted by the different isotherm models as described in the previous section. The resulting acceptable models are assembled in Table 13.

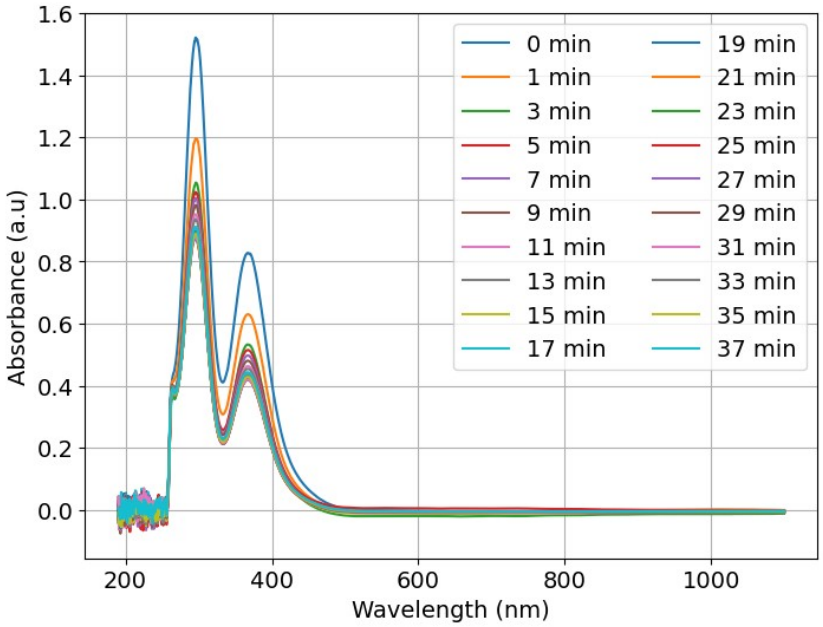

Figure 19: Time-resolved UV-Vis absorption spectra for the stoichiometry of PVIm:SWCNT (7:1)

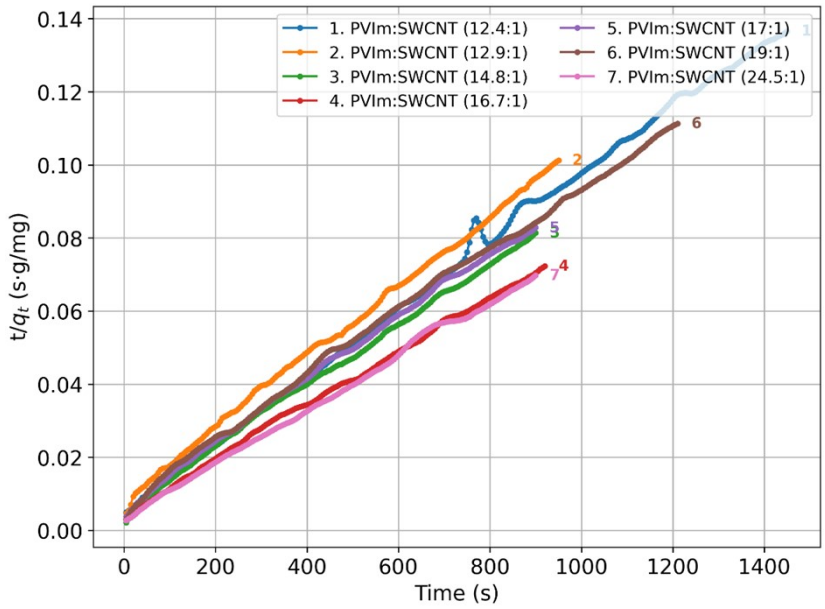

Figure 20: : Quantity t/qt plotted as a function of t, for different PVIm:SWCNT stoichiometry. Only the linear range for each stoichiometry is displayed here

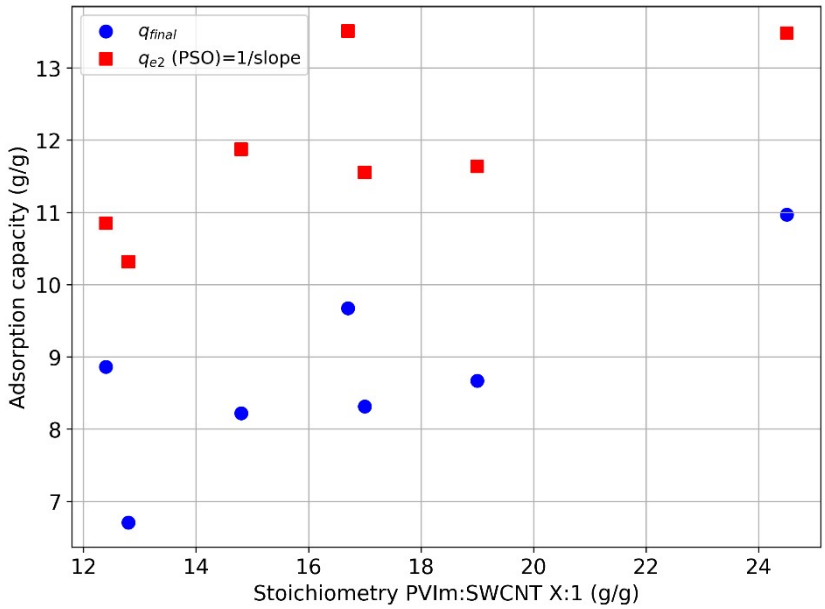

Figure 21: Equilibrium adsorption capacity qe_2 (derived from the pseudo second order kinetics) and final adsorption capacity q_{final} (average of q_t over the last 50 s of the kinetics) as a function of PVIm:SWCNT stoichiometry.

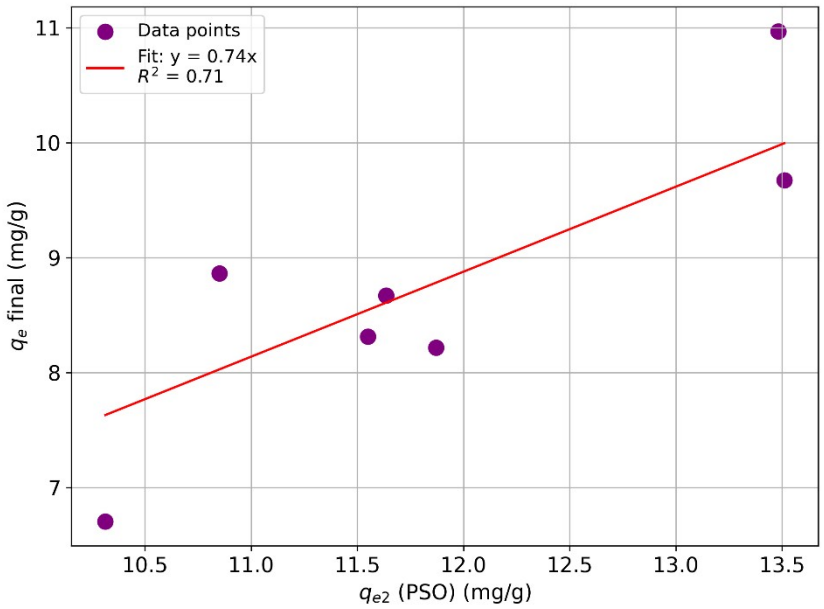

Figure 22: Linear trend between the equilibrium adsorption capacity qe_2 and the final adsorption capacity q_{final}.

Table 12: Kinetic parameters for adsorption of PVKIm on SWCNTs. R^2 is the correlation coefficient for the linear fit of t/qt as a function t; q_{final} and dq_{final} are respectively the average and the standard deviation of qt over the last 50s of the kinetics experiment; q_{e2} and k_2, and the corresponding uncertainties dq_{e2} and k_2, are derived from the linear fit of t/q_t. The initial slope $dq_t/dt(t=0)$ is derived by linear fit of qt as a function of t over the initial 15 s to 30 s of the kinetics.

Stoichiometry PVIm:SWCNT X:1	12,4	12,8	14,8	16,7	17	19	24,5
Initial PVImconcentration (ppm)	39	41	47	53	54	60	78
R^2	0,999	0,999	0,998	0,999	0,998	0,998	0,998
q_{final} (mg/g)	8860	6700	8220	9670	8310	8670	11100
dq_{final}/q_{final} (%)	1.9%	0.31%	0.21%	0.25%	0.23%	0.19%	0,29%
initial gradient dqt/dt(t=0) (mg/g/s)	145	108	274	259	197	216	301
q_{e2} (mg/g)	10900	10300	11900	13500	11600	11600	13500
k_2 (g/mg.s)	1,6E-6	1,1E-6	1,2E-6	1,2E-6	1,1E-6	9,2E-7	1,6E-6
dq_{e2}/qe_2 (in %)	0,21	0,25	0,31	0,28	0,29	0,27	0,33
dk_2/k_2 (in %)	3,46	2,07	2,92	2,88	2,55	2,59	4,45

Table 13: Fitting of q_e=q_{final} as a function of the initial PVIm concentration C_e by different isotherm models, accounting for the uncertainties on q_{final} and C_e. Only the models with moderate (<<100 %) coefficient of variations are listed.

Model	***Name of the parameter***	***Isotherm Parameters***	***R^2***	*MAPE*	***MAE (g/g)***
Freundlich $q_e = K_f C_e^{1/n}$	*K_f (g/g.ppm$^{-1/n}$)* *n*	1.4 ± 30 % 2.1± 17 %	0.56 ± 20 %	8.5 % ± 16 %	0.72 ± 17 %
Temkin $q_e = \frac{RT}{b}\ln(K_{Te}C_e)$	*K_{Te} (ppm^{-1})* *RT/b (g/g)*	0.18 ± 41 % 4200 ± 15 %	0.54 ± 20 %	8.8 % ± 15 %	0.75 ± 15 %
Langmuir $q_e = \frac{q_m a_L C_e}{1 + a_L C_e}$	*q_m (g/g)* *a_L (ppm)*	18 ± 16 % 0.021 ± 32 %	0.54 ± 23 %	8.7 % ± 16 %	0.74 ± 16 %
Langmuir linearized $q_e = q_m(1 - \frac{1}{a_L C_e})$	*q_m (g/g)* *a_L (ppm)*	13 ± 5.5 % 0.062 ± 12 %	0.50 ± 24 %	9.4 % ± 16 %	0.80 ± 17 %
Dubinin–Radushkevich $q_e = q_m \exp - \frac{(RT\ln(1 + 1/C_e))^2}{2E^2}$	*q_m (g/g)* *E (kJ/mol)*	11 ± 4.4 % 640 ± 18 %	0.48 ± 26 %	9.5 % ± 15 %	0.81 ± 16 %
Dubinin–Radushkevich linearized $q_e = q_m(1 - \frac{(RT)^2}{2E^2}\frac{1}{C_e^2})$	*q_m (g/g)* *E (kJ/mol/ppm)*	11 ± 3.6 % 0.47 ± 16 %	0.45 ± 28 %	9.8 % ± 16 %	0.84 ± 16 %

S12 FTIR data of the SWCNTs

Figure 23 shows the FTIR spectrum of the SWCNTs, acquired according to the process detailed in Section 2.2.5. Peaks were marked and attributed based on Devaux et al. for high-level assignation by range of wavelengths and on Bantignies et al. for assignation of SWCNT (D band, tangential, radial, or derived from modes of graphite) and amorphous carbon peaks [2,3]. Overall, the data are consistent with pristine HiPcO SWCNTs, showing with very few carboxyl defects and possible signs of amorphous carbon.

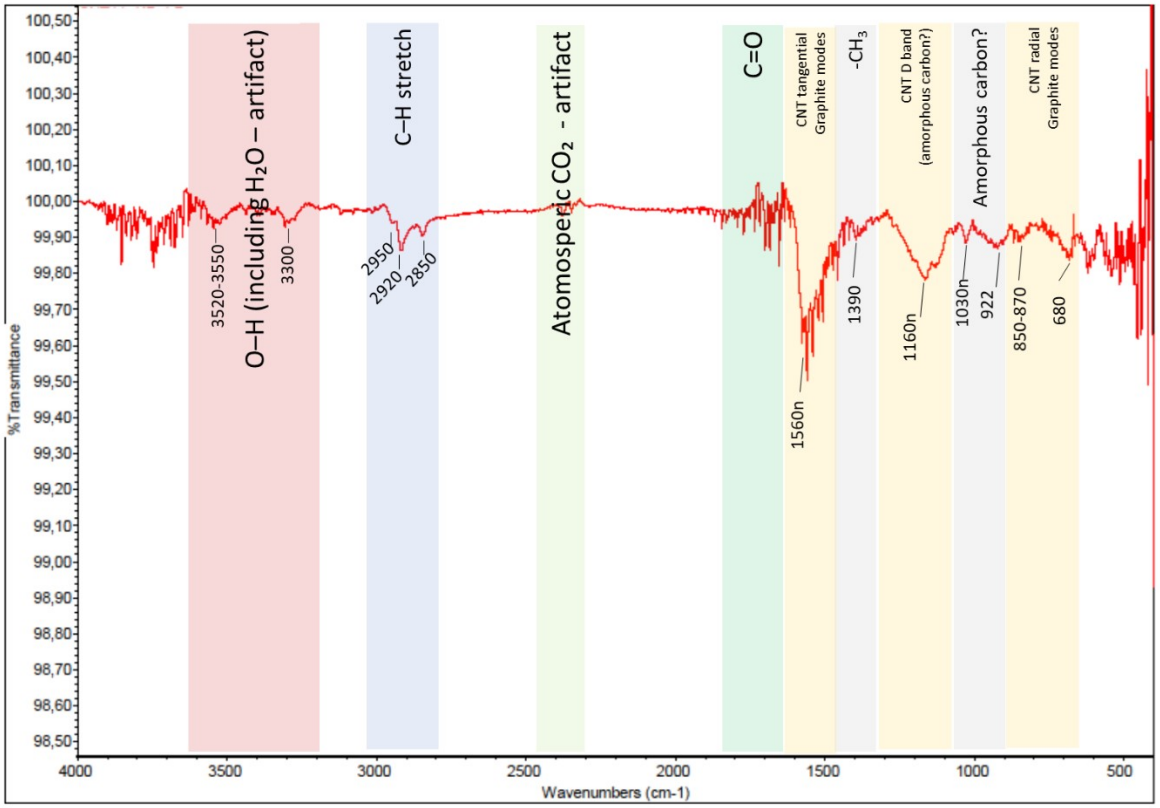

Figure 23: FTIR Spectrum of pristine SWCNT

S13 XPS results

A set of 5 samples was tested with XPS according to the protocol described in Section 2.2.6. The samples tested were pure SWCNTs, PVT, PVKdac, PVT:SWCNT 1.2:1, and PVKdac:SWCNT 1.7:1, all dispersed in NMP.

Table 15 shows the elemental composition of the samples. The presence of Fe in the samples containing SWCNTs is consistent with the TEM results discussed in Section 3.1.2. The presence of N atoms is due to both the polymers and the NMP. Considering the N/O and N/C ratio relative to the compositions of the different samples, the N concentration was much lower than expected, suggesting carbon contamination. This finding is consistent with the presence of Cl in some of the samples at non-negligible concentration, which is often attributed to organic contamination. Due to the presence of contamination, significant care was taken in attributing and interpreting the deconvoluted C1s peaks, as detailed in the following paragraphs.

Table 15: Atomic compositions in %. NB: due to the effect of the round up to 2 significant digits, the sum does not reach exactly 100%

Samples Atom	SWCNT	PVT	PVKdac	PVKdac:SWCNT	PVT:SWCNT
C	76	86	84	85	83
Cl	2.0	2.5	4.7	0.73	2.3
Fe	0.37	-	-	0.27	-
N	3.2	2.5	2.6	3.8	4.1
O	14	9.0	7.9	10	9.0
Si	4.3	0.26	1.0	0.17	1.4

Deconvolution of the C1s peak between 280 and 292 eV was achieved using version 1.65_25j10 of the KherveFitting software. After automated background removal (using the "Smart" method with 5 averaging points) [4], the selected fitting model for deconvolution was "SGL (Area)" with the least squares method, uniform weights, and 20 iterations (default parameters). Initially, a three-peak decomposition (peak 1: C-C and C=C; peak 2: C-N, C-Cl, and C-O; peak 3: C=O and N-C=O) was tested with satisfactory fitting performance, as recommended by Gengenbach et al. to prevent overfitting [5]. However, the presence of NMP (Figure 24, left) and carbon contamination in most samples affected the 3 peaks, hiding the contributions of the polymers and of the SWCNTs. As an alternative, a deconvolution up to 5 peaks was tested for each sample. To avoid overfitting, the following process was implemented. A first fit with 5 peaks was carried out. Then peaks that 1) had a negligible area (below a 0.1% contribution), or 2) were very close in wavelength to another peak (within ±0.2

eV), or 3) had no reasonable chemical correspondence were removed one by one and the fit recalculated each time. Correspondences were interpreted based on the information in Figure 24 (right) and in Chen et al. [6] . Figure 25 to Figure 29 present the resulting deconvolutions of the C1s peaks for the 5 samples. Table 16 presents the quantitative peaks information and tentative attribution, and Table 17 provides a comparative analysis of the N-C=O peak of NMP across all samples.

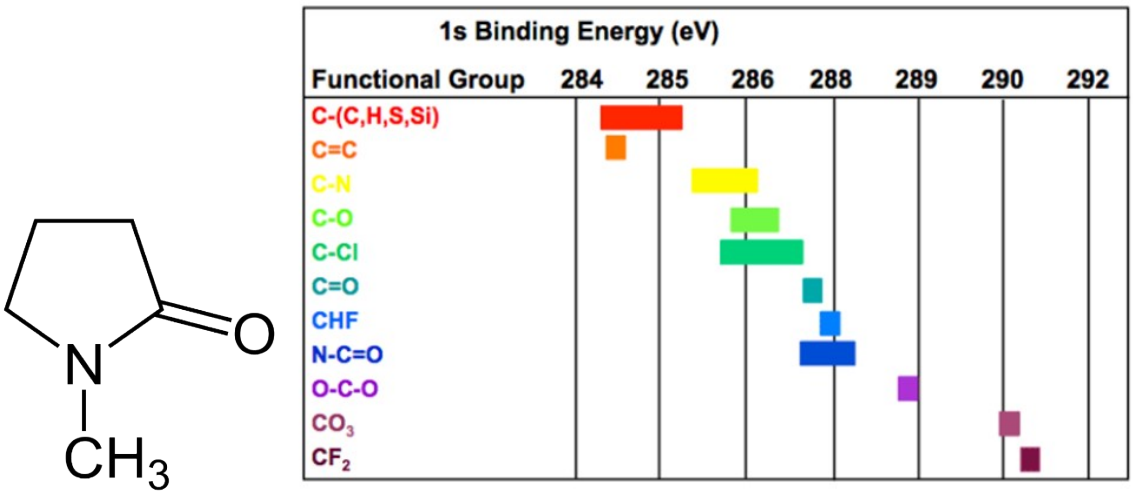

Figure 24: Left: Formula of NMP. Right: C1s binding shifts according to functional groups. Reproduced from [7].

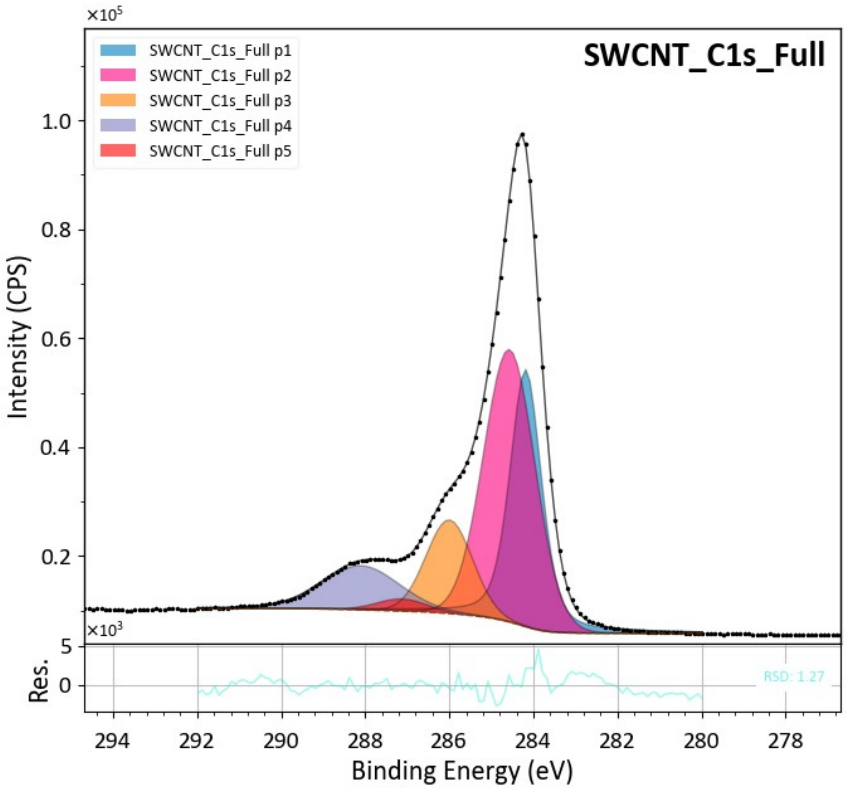

Figure 25: 5-peak deconvolution of the SWCNT C1s peak

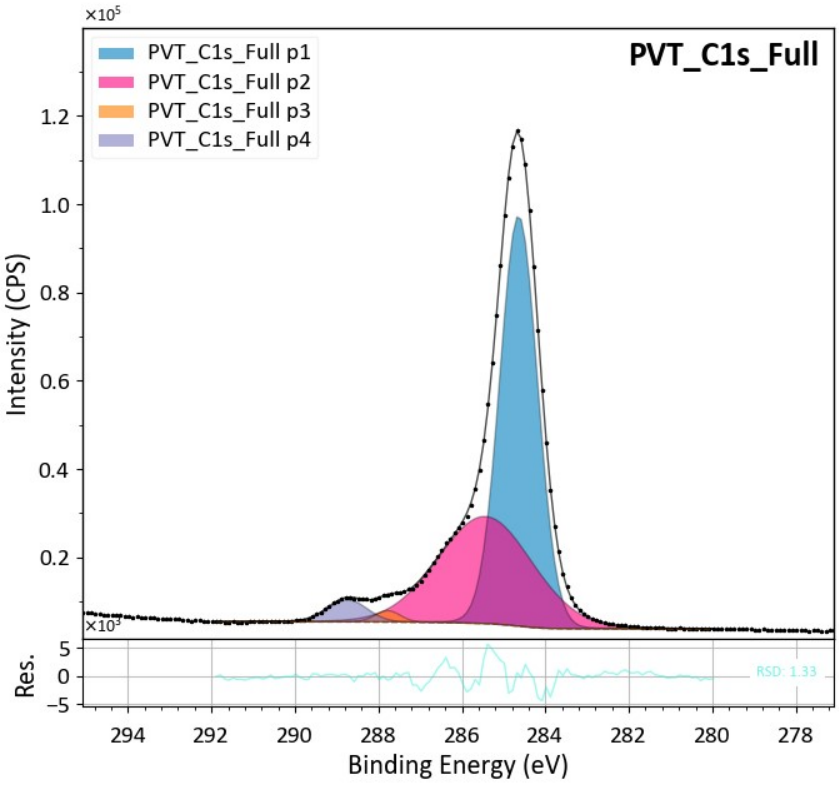

Figure 26: 4-peak deconvolution of the PVT C1s peak

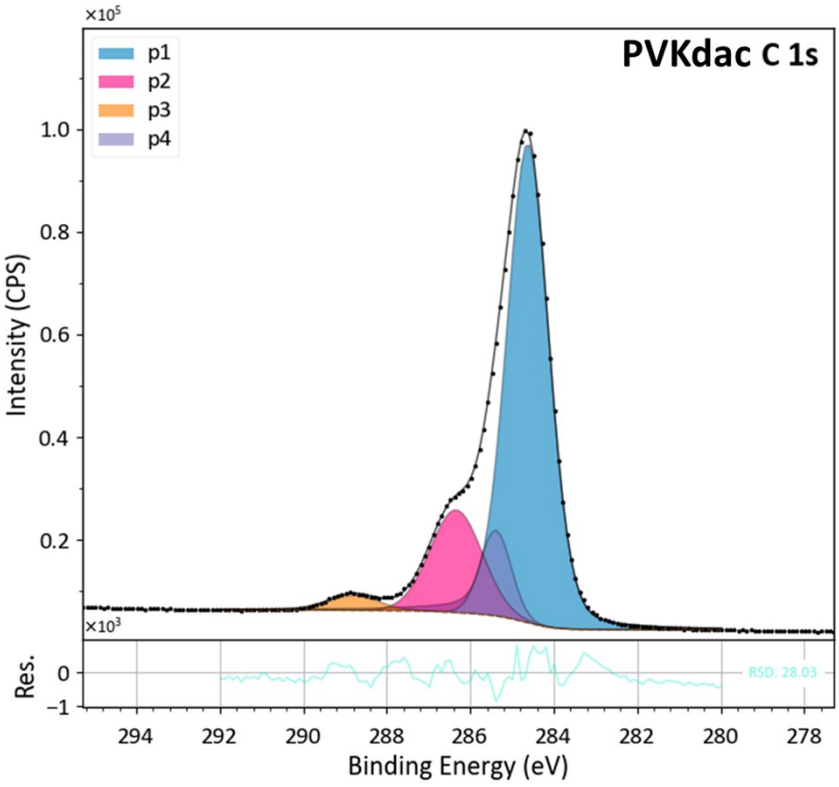

Figure 27: 4-peak deconvolution of the PVKdac:SWCNT C1s peak (stoichiometry 1.2:1)

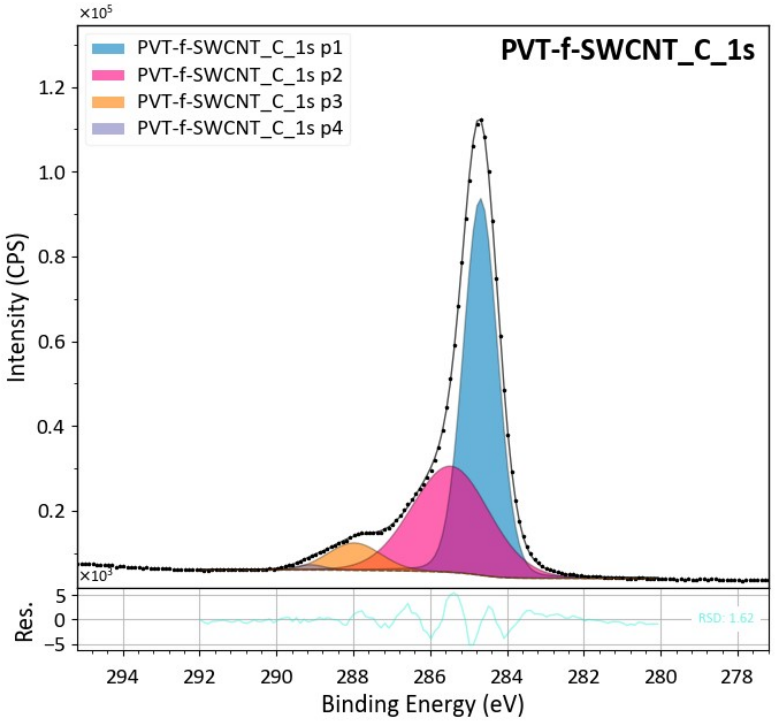

Figure 28: 4-peak deconvolution of the PVT:SWCNT C1s peak (stoichiometry 1.2:1)

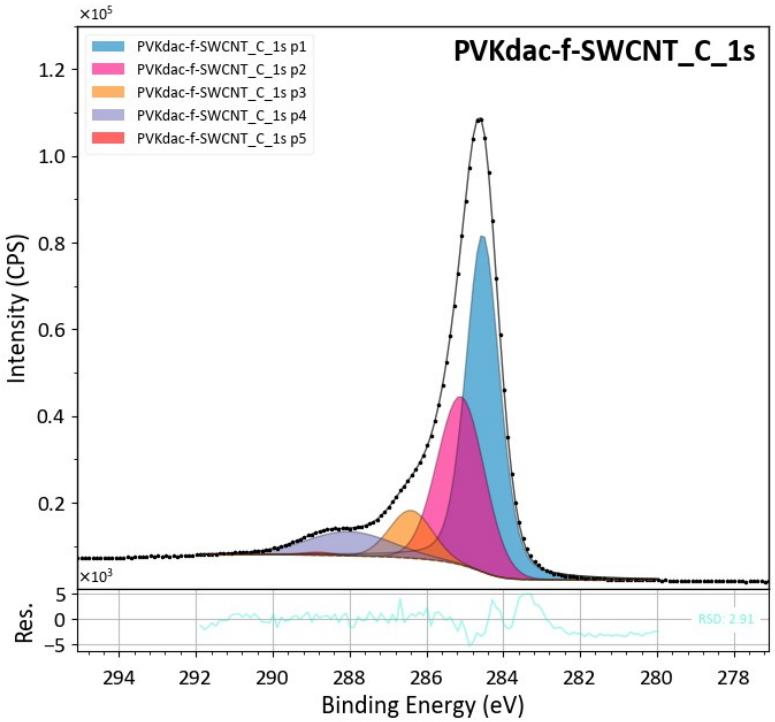

Figure 29: 5-peak deconvolution of the PVKdac:SWCNT C1s peak (stoichiometry 1.7:1)

Table 16: Results of the deconvolution of the C1s peak of the 5 samples. The colour code marks the peaks assumed to be of the same origin in the different samples

Peak Label	Position (eV)	FWHM (eV)	Conc. (%)	Tentative identification	Contributing material
SWCNT					
p1	284.18	0.88	29.8	C=C	CNT
p2	284.57	1.44	43.6	C-C	NMP ; contamination
p3	286.00	1.30	13.6	C-O	Contamination
p5	287.13	1.41	2.0	C-Cl	Contamination
p4	288.10	2.16	11.1	N-C=O	NMP
PVT					
p1	284.64	1.06	57.6	C-C	PVT ; NMP & contamination (reduced amount)
p2	285.44	2.66	38.1	C-N	PVT
p3	287.78	0.71	1.1	N-C=O	NMP (reduced amount)
P4	288.74	1.10	3.2	C=O	Contamination (reduced amount)
PVK					
p1	284.62	1.19	71.4	C=C	PVKdac
p4	285.39	0.87	8.7	C-C	PVKdac ; possible contamination
p2	286.34	1.47	17.5	C-N	PVKdac
p3	288.78	1.36	2.4	C=O	PVKdac ; possible contamination
PVT:SWCNT (stoichiometry 1.2:1)					
p1	284.69	1.05	57.3	C-C	PVT ; NMP ; contamination
p2	285.47	2.38	35.8	C-N	PVT
p3	287.98	1.63	6.2	N-C=O	NMP
P4	289.13	0.89	0.7	C=O	Contamination (reduced amount)
PVKdac:SWCNT (stoichiometry 1.7:1)					
p1	284.53	1.04	51.5	C=C	PVKdac
p2	285.10	1.44	31.6	C-C	PVKdac ; NMP ; contamination
p3	286.40	1.31	8.2	C-N	PVKdac
p4	288.01	2.63	8.3	N-C=O	NMP
p5	288.82	0.97	0.4	C=O	Contamination (reduced amount)

Table 17: Synthesis of the parameters of the N-C=O peak corresponding to NMP

Peak Label	Position (eV)	FWHM (eV)	Conc. (%)	Tentative identification	Contributing material
SWCNT	288.10	2.16	11.1	N-C=O	NMP
PVT	287.78	0.71	1.1	N-C=O	NMP
PVKdac	Absent from C1s peak				
PVT:SWCNT (stoichiometry 1.2:1)	287.98	1.63	6.2	N-C=O	NMP
PVKdac:SWCNT (stoichiometry 1.7:1)	288.01	2.63	8.3	N-C=O	NMP

The results of the SWCNT deconvolution suggest that the C1s spectrum is controlled by the CNT C=C peak (30%; at the lower end of the acceptable wavelength range), the NMP N-C=O peak (11%), and the C-C peak, which is largely contributed by the NMP and slightly by the organic contamination. The absence of the C=O peak (which can be seen in the other spectra) suggests that CNT defects (C-C and C=O peaks) contribute negligibly to the spectrum compared to the contributions of the NMP and organic contamination.

The PVT spectrum shows a much lower NMP peak contribution and a significant C=O peak presence, confirming organic contamination. This contamination is expected to influence the C-C peak. The PVKdac spectrum shows no sign of the NMP N-C=O peak and a C=O peak that may be due to C=O bonds in PVKdac. While possible, the contribution of organic contamination to the C1s peak of PVKdac cannot be confirmed.

The PVT:SWCNT sample shows four peaks at wavelengths similar to those of the PVT sample. The C-C and C-N peaks of the PVT:SWCNT hybrid are within ±0.05 eV of the C-C and C-N peaks of PVT alone and have a similar width and percentage composition. The absence of the C=C peak of the SWCNT suggests that the XPS beam does not reach the SWCNTs within the PVT sheath. The absence of noticeable modification to the C-C and C-N peaks, on the other hand, indicates that any electronic or conformal influence of the SWCNTs inside the PVT sheath does not reach the outer layer of the PVT sheath (the one reached by the XPS beam). In other words, this data suggests that the PVT layer fully covers the SWCNT and is thicker than the XPS beam's penetration depth in PVT. This finding is consistent with the AFM images in section 3.1.1 of the main text.

The PVKdac:SWCNT sample shows 5 peaks: the 4 PVKdac peaks and the N-C=O peak of the NMP. The C=C and C-N peaks of PVKdac are maintained with very similar wavelengths (±0.05 eV) and width, and there is no sign of the C=C peak of the SWCNTs. The wavelength of the C-C peaks changes slightly, which may be due to the increased presence of NMP (absent from the PVKdac spectrum and present in the PVKdac:SWCNT spectrum). This suggests interpreting these peaks simiarly to the PVT interpretation: each SWCNT is fully wrapped in a thick layer of PVKdac.

Interestingly, unlike the C-C, C-N and C=C peaks, the N-C=O peak shows significant variation from sample to sample, as illustrated in Table 17. Its absence in the PVKdac spectrum, coupled with its narrow shape and low intensity in the PVT spectrum, suggests weak interaction between the two polymers and the NMP molecule. Conversely, the wide, intense NMP peak in

the SWCNT sample, which is at a higher wavelength than in the PVT samples, suggests the presence of NMP molecules in various conformations in the pure SWCNT sample, probably as free molecules (non-evaporated during the drying process) and SWCNT-bound ones (eg., adsorbed). The N-C=O peak of the NMP in the two functionalized samples has a similar wavelength and width to the SWCNT one. It is unlikely that these NMP molecules in the polymer:SWCNT samples are simply trapped at the SWCNT/polymer interface, considering that the XPS beam does not reach the SWCNTs. Similarly, the hypothesis that these are free NMP molecules outside the polymer layer (as in the free PVT and PVKdac samples) is also unlikely, given the differences in the shape and wavelengths of the NMP peaks. The remaining hypothesis is that the N-C=O peaks in the polymer:SWCNT spectra corresponds to NMP molecules trapped within the thick polymer layer around the SWCNTs. In other words, the XPS data suggest that the polymer layer around the SWCNTs is somewhat porous and filled with a significant amount of NMP (6-8 % of the carbon content of the material investigated by the beam).

S14 Carbon footprint calculation

The process described in the paper could be used, for example, to reduce the carbon footprint of PVC waste incineration. The direct CO_2 emission from PVC incineration is over 1.8 kg of CO_2 per kg of PVC [8]. It accounts for over 10 % of PVC waste, or over 6 million tons per year in the EU alone.

Let us assume that, instead of incinerating PVC waste, it is dissolved in an appropriate solvent. Using the process described in this paper, the dissolved PVC adsorbs onto SWCNTs, which are then used to reinforce concrete materials. The following paragraphs explain why this strategy would have a positive CO_2 impact.

The global warming impact of the SWCNTs is offset by their use in concrete reinforcement. In fact, the current estimate of the global warming impact of SWCNT production is slightly higher than 10 kg of CO_2 per kg of SWCNTs for the two large-scale inventories reported in Temizel-Sekeryan et al. [9]. Conversely, adding less than 0.1 wt% of CNTs to concrete (1 kg of CNTs per ton of concrete) has often been reported to increase its strength by over 10 %, which translates to a reduction of over 10 % in the volume of concrete needed. With a global warming impact of 200 kg of CO_2 per ton of concrete, using 1 kg of SWCNTs reduces CO_2 by 20 kg, a number comparable to the production cost of the SWCNTs themselves. For example, Licht et al. report an even more favorable number regarding CO_2 [10]: "a 2-ton cement block with 0.001 tons of CNTs has the same strength as a 3-ton block without CNTs. The 1-ton cement avoided eliminates its CO_2 production emissions. Specifically, a 0.048 wt% CNT-cement composite eliminates 840 tons of CO_2 per ton of CNTs".

The global warming impact of dispersing SWCNTs is more than offset by the impact of not incinerating PVC, leaving a significant margin for reducing the CO_2 footprint. Assuming 10 g of PVC is adsorbed PVC per g of SWCNTs, 1kg of PVC requires 100 g of SWCNTs for full adsorption. The latter requires dispersion in approximately 1 m3 of solvent at the concentrations tested in this paper. Since all processes are caried out at room temperature, the most energy-intensive part of the process is centrifugation. Pessimistic estimates of the energy consumption of centrifugation at 10,000 *g* for 5 hours are 50 kWh/m^3. In France, the CO_2 equivalent of 1 kWh is ~0.01 kg CO_2, yielding a CO_2 cost for the centrifugation operation of 0.5 kg CO_2/m^3, well below the 1.8 kg of CO_2 per kg of PVC cost of incinerating PVC, leaving a margin of 1.3 kg of CO_2 per kg of PVC [11].

Naturally, there are many direct or indirect CO_2 costs that are not yet known, so these numbers are very rough. However, they suggest the potential positive impact of the proposed technology on reducing environmental CO_2.

References

[1] M.A. Al-Ghouti, D.A. Da'ana, Guidelines for the use and interpretation of adsorption isotherm models: A review, Journal of Hazardous Materials 393 (2020) 122383. https://doi.org/10.1016/j.jhazmat.2020.122383.

[2] X. Devaux, B. Vigolo, E. McRae, F. Valsaque, N. Allali, V. Mamane, Y. Fort, A.V. Soldatov, M. Dossot, S.Yu. Tsareva, Covalent Functionalization of HiPco Single-Walled Carbon Nanotubes: Differences in the Oxidizing Action of H2SO4 and HNO3 during a Soft Oxidation Process, ChemPhysChem 16 (2015) 2692–2701. https://doi.org/10.1002/cphc.201500248.

[3] J.-L. Bantignies, J.-L. Sauvajol, A. Rahmani, E. Flahaut, Infrared-active phonons in carbon nanotubes, Phys. Rev. B 74 (2006) 195425. https://doi.org/10.1103/PhysRevB.74.195425.

[4] Kerherve, Gwilherm, William S. J. Skinner, Julian A. Hochhaus, Arthur Graf , David J. Morgan, Mark A. Isaacs, Benjamen P. Reed, Hideki Nakajima, David J. Payne., An open-source software for fitting X-ray photoelectron spectroscopy data, Accepted for Publication in Surface and Interface Analysis, DOI Pending (2025).

[5] T.R. Gengenbach, G.H. Major, M.R. Linford, C.D. Easton, Practical guides for x-ray photoelectron spectroscopy (XPS): Interpreting the carbon 1s spectrum, J. Vac. Sci. Technol. A 39 (2021) 013204. https://doi.org/10.1116/6.0000682.

[6] X. Chen, X. Wang, D. Fang, A review on C1s XPS-spectra for some kinds of carbon materials, Fullerenes, Nanotubes and Carbon Nanostructures 28 (2020) 1048–1058. https://doi.org/10.1080/1536383X.2020.1794851.

[7] S. Mitchell, XPS provides chemical bond information, EAG Laboratories (2020). https://www.eag.com/app-note/xps-provides-chemical-bond-information/ (accessed November 16, 2025).

[8] K A BROWN, M R HOLLAND, R A BOYD, S THRESH, H JONES, S M OGILVIE, Economic Evaluation of PVC Waste Management, European Commission Environment Directorate, 2000. https://ec.europa.eu/environment/pdf/waste/studies/pvc/economic_eval.pdf.

[9] S. Temizel-Sekeryan, F. Wu, A.L. Hicks, Global scale life cycle environmental impacts of single- and multi-walled carbon nanotube synthesis processes, Int J Life Cycle Assess 26 (2021) 656–672. https://doi.org/10.1007/s11367-020-01862-1.

[10] S. Licht, X. Liu, G. Licht, X. Wang, A. Swesi, Y. Chan, Amplified CO2 reduction of greenhouse gas emissions with C2CNT carbon nanotube composites, Materials Today Sustainability 6 (2019) 100023. https://doi.org/10.1016/j.mtsust.2019.100023.

[11] Our emissions in mainland France | EDF FR, (2025). https://www.edf.fr/groupe-edf/agir-en-entreprise-responsable/responsabilite-societale-d-entreprise/rapports-et-indicateurs/emissions-de-gaz-a-effet-de-serre/nos-emissions-en-france-continentale (accessed November 16, 2025).